

Article

Mineralogical Constraints on the Potassic and Sodic-Calcic Hydrothermal Alteration and Vein-Type Mineralization of the Maronia Porphyry Cu-Mo \pm Re \pm Au Deposit in NE Greece

Vasilios Melfos ^{1,*}, Panagiotis Voudouris ², Margarita Melfou ¹, Matías G. Sánchez ³, Lambrini Papadopoulou ¹, Anestis Filippidis ¹, Paul G. Spry ⁴, Anna Schaarschmidt ⁵, Reiner Klemm ⁵, Karsten M. Haase ⁵, Alexandre Tarantola ⁶ and Constantinos Mavrogenatos ²

¹ Department of Mineralogy, Petrology and Economic Geology, Aristotle University of Thessaloniki, 54124 Thessaloniki, Greece; margaritamelfou@gmail.com (M.M.); lambrini@geo.auth.gr (L.P.); anestis@geo.auth.gr (A.F.)

² Department of Mineralogy-Petrology, National and Kapodistrian University of Athens, 15784 Athens, Greece; voudouris@geol.uoa.gr (P.V.); kmavrogen@geol.uoa.gr (C.M.)

³ Fault Rocks Inc., Vancouver, BC V6G 1M8, Canada; msanchez@faultrocks.com

⁴ Department of Geological and Atmospheric Sciences, Iowa State University, Ames, IA 50011, USA; pgspry@iastate.edu

⁵ GeoZentrum Nordbayern, Friedrich-Alexander-Universität (FAU) Erlangen-Nürnberg, Schlossgarten 5, 91054 Erlangen, Germany; anna.schaarschmidt@fau.de (A.S.); reiner.klemm@fau.de (R.K.); karsten.haase@fau.de (K.M.H.)

⁶ GeoRessources, Faculté des Sciences et Technologies, UMR Université de Lorraine, 54506 Nancy, France; alexandre.tarantola@univ-lorraine.fr

* Correspondence: melfosv@geo.auth.gr

Received: 18 January 2020; Accepted: 16 February 2020; Published: 18 February 2020



Abstract: The Maronia Cu-Mo \pm Re \pm Au deposit is spatially related to a microgranite porphyry that intruded an Oligocene monzonite along the Mesozoic Circum-Rhodope belt in Thrace, NE Greece. The magmatic rocks and associated metallic mineralization show plastic and cataclastic features at the south-eastern margin of the deposit that implies emplacement at the ductile-brittle transition, adjacent to a shear zone at the footwall of the Maronia detachment fault. The conversion from ductile to brittle deformation caused a rapid upward magmatic fluid flow and increased the volume of water that interacted with the host rocks through high permeable zones, which produced extensive zones of potassic and sodic-calcic alteration. Potassic alteration is characterized by secondary biotite + K-feldspar (orthoclase) + magnetite + rutile + quartz \pm apatite and commonly contains sulfides (pyrite, chalcopyrite, pyrrhotite). Sodic-calcic alteration consists of actinolite + sodic-calcic plagioclase (albite/oligoclase/andesine) + titanite + magnetite + chlorite + quartz \pm calcite \pm epidote-allanite. The high-oxidation state of the magmas and the hydrothermal fluid circulation were responsible for the metal and sulfur enrichments of the aqueous fluid phase, an increase in O₂ gas content, the breakdown of the magmatic silicates and the production of the extensive potassic and sodic-calcic alterations. Brittle deformation also promoted the rapid upward fluid flow and caused interactions with the surrounding host rocks along the high temperature M-, EB-, A- and B-type veins.

Keywords: porphyry deposit; potassic alteration; sodic-calcic alteration; vein-types; Maronia; Greece

1. Introduction

Hydrothermal alteration in porphyry type deposits refers to modifications in the primary chemistry, mineralogy and texture of the host rocks in response to fluid-rock interactions [1–3]. Porphyry systems are characterized by several alteration mineral assemblages, which are distributed in zones with a kilometer-scale lateral and vertical extent, as part of the evolving magmatic-hydrothermal system. Various factors control the geometry of these zones and the intensity of the alteration, including: nature of the ascending magmas, nature of the circulating fluids, rock composition, temperature, pressure and orientation of large tectonic structures, which form permeable conduits for hydrothermal fluids.

According to Lowell and Gilbert [4], Beane and Titley [5], Sinclair [6], Seedorff et al., [2] and Sillitoe [3], early magmatic fluids with high temperature (>350 °C) interact with the host-rocks forming sodic-calcic and potassic alteration zones in the core of ore forming systems, whereas propylitic alteration zones generally occur at the periphery. Late meteoric waters commonly mix with magmatic fluids and react with the wall rocks resulting in sericitic and argillic alterations at lower temperatures. Several hydrothermal minerals, such as actinolite, calcite, biotite, epidote, chlorite, kaolinite, K-feldspar, magnetite, sericite and titanite, replace earlier-formed primary magmatic minerals, and are indicators of the various alteration zones in porphyry Cu deposits [3].

The identification of the hydrothermal alteration zones, especially potassic and chlorite-sericitic, is important for the exploration and reconnaissance of porphyry systems, as they are commonly spatially associated with economic sulfide mineralization [3]. The significance of potassic alteration is strengthened by Kesler et al. [7], who stated that it is the main repository of Au in porphyry deposits, either as small inclusions in bornite or as overgrowths on it.

The Rhodope magmatic-metallogenic belt in northern Greece includes numerous Oligocene-Miocene porphyry type deposits (Figure 1). They are linked with magma emplacement along detachment faults and the exhumation of metamorphic core complexes in back-arc settings [8,9]. Characteristic examples occur in Thrace (Maronia, Pagoni Rachi, Konos, Kassiteres, Myli, Aisymi-Leptokarya, Melitena), Chalkidiki (Skouries, Fisoka, Dilofo, Tsikara), Kilkis (Doirani, Vathi, Gerakario), Limnos island (Sardes, Fakos) [9], and Lesvos island (Stypsi) [10].

The Maronia porphyry Cu-Mo ± Re ± Au deposit was previously studied by Melfos et al. [11] in terms of geology, magmatism, hydrothermal alteration, ore mineralogy and fluid inclusions for metallogenic interpretations. However, the potassic and sodic-calcic hydrothermal alterations had not been evaluated and were recognized later, during recent field studies. These studies were in line with the presence of potassic and sodic-calcic alterations in several other porphyry-style mineralized prospects in the eastern Rhodope area (e.g., Koryfes, Papadokoryfi, Pagoni Rachi, King Arthur, Myli) by Voudouris et al. [11–16] and Mavrogonatos et al. [17].

In this contribution, we present the distribution patterns, textural relationships and chemical composition of hydrothermal minerals in the potassic and sodic-calcic alterations of the Maronia porphyry system. The study aims to understand the association of the early high temperature alterations and the evolution of the porphyry system in one of the most promising metallogenic belts of south-eastern Europe, spatially associated with the Rhodope massif. Identification of potassic and sodic-calcic hydrothermal alteration zones may provide useful exploration vectors as they may point toward undiscovered parts of the deposits [18,19]. Based on field observations and a mineralogical study, we prepared new geological and hydrothermal alteration maps from pre-existing geological maps of the area [11], complemented by new field observations and mineralogical analyses.

2. Geological Setting

The Cenozoic metallogeny of Greece was influenced by the geodynamic evolution of the Western Tethyan Metallogenic Belt, which formed as a result of the opening and closing of the Vardar and Pindos oceanic domains of the Tethys Ocean between the Eurasia and African plates [8,20]. Subduction of oceanic lithosphere below the Eurasian margin began near Apuseni Mountains and the Banat area in Romania during the Late Jurassic and progressively migrated to the south, through Srednogie

and the Rhodope, in Bulgaria and Greece [20–24]. Today, the subduction is located below the South Aegean Active Volcanic Arc.

Above this southward migrating subduction zone, multistage magmatic complexes and associated metal deposits developed in a post-collisional extensional regime during the Cenozoic. The evolving subduction-related processes included slab retreat and tearing, upwelling of asthenospheric mantle and melting during back-arc extension, generation and emplacement of magmas and subsequent metals in arc and back-arc environments and orogenic collapse along large scale detachment faults that exhumed metamorphic core complexes [9,20,25–27]. The latter are located in the Rhodope massif and the Vertsikos unit of the Serbo-Macedonian massif in northern Greece (Figure 1).

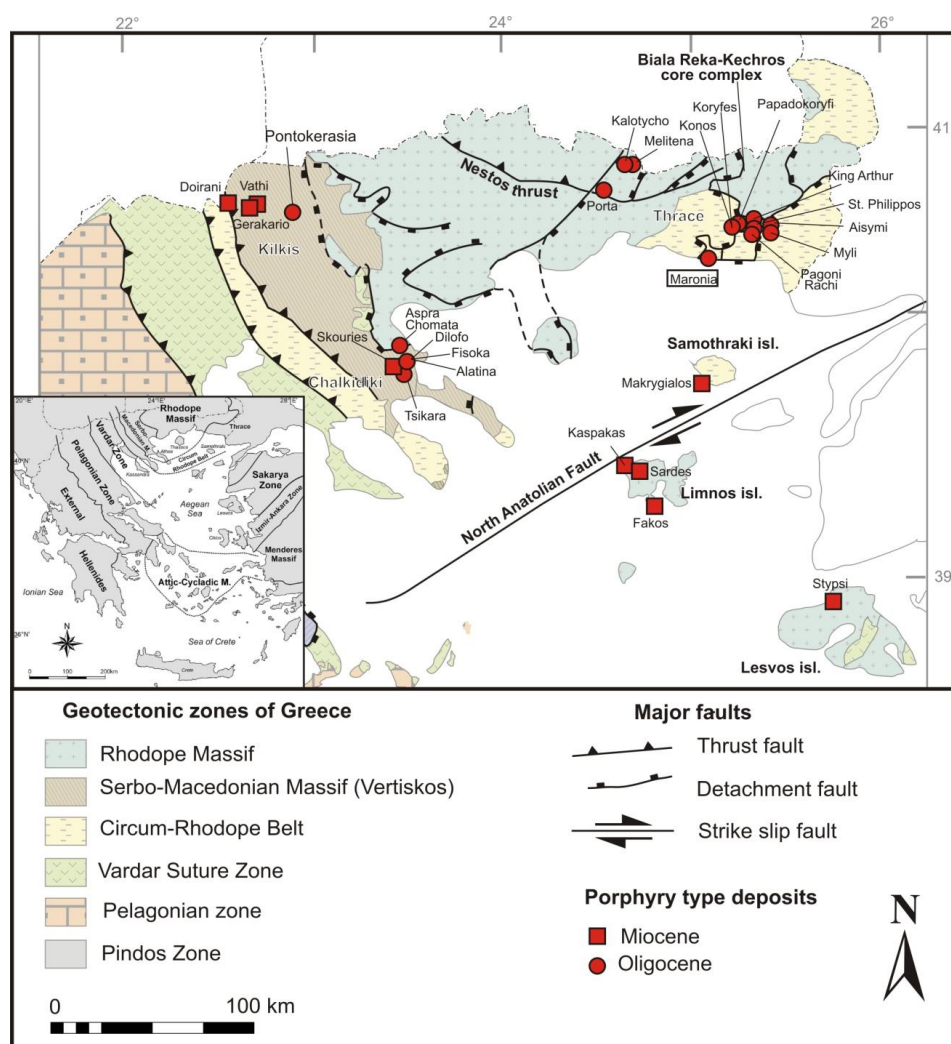


Figure 1. Simplified map of Northern Greece showing the main geotectonic zones, the major tectonic structures within the Hellenides, and the distribution of porphyry-type deposits (after Melfos and Voudouris [8]; Voudouris et al. [9]). The Maronia area is outlined and the geotectonic zones of the Hellenic orogen are shown in the inset.

In this region, numerous porphyry Cu-Mo ± Au ± Re deposits formed from calc-alkaline to shoshonitic magmas derived from partial melting of previously subduction-modified sub-lithospheric mantle and/or the lower crust [8,9]. The deposits are distributed around metamorphic core complexes bound by low-angle detachment faults. Such faults promoted the ascent of magmas and the circulation of hydrothermal fluids, which ultimately resulted in the formation of the porphyry-style mineralization.

One of these porphyry-type deposits occurs in the Rhodope massif, 5 km SE of Maronia village, along the Aegean coast (Figures 1 and 2). The geological setting of the area is characterized by the low metamorphic grade Mesozoic Circum Rhodope metamorphic belt, which overlies the upper unit of the Paleozoic-Mesozoic high-grade metamorphic basement of the Rhodope massif [28,29]. The Circum Rhodope belt comprises metasedimentary (metaconglomerates, metagreywackes, metaquartzites, marbles, calc-schists) and metavolcanic rocks (greenschists, chlorite schists, talc schists, mica schists, quartzites) of Triassic to Jurassic protolith age.

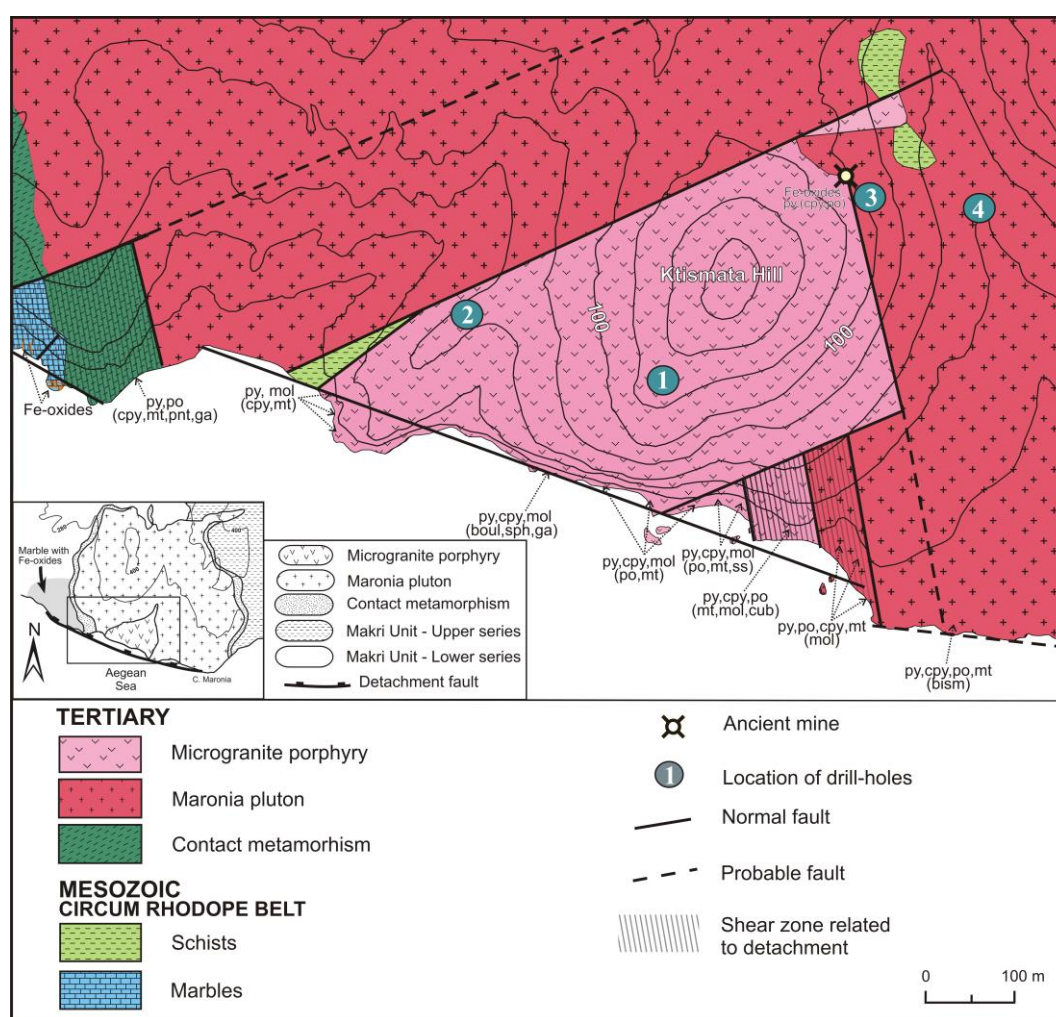


Figure 2. Geological sketch map of the porphyry Cu-Mo-Re \pm Au deposit of Maronia showing the mineralization occurrences (modified from [11]). mt: magnetite; py: pyrite; po: pyrrhotite; pnt: pentlandite; cpy: chalcopyrite; mol: molybdenite; sph: sphalerite; ga: galena; cub: cubanite; bism: bismuthinite; boul: boulangerite; ss: Cu-Pb-(Sb + As) sulfosalts (bournonite, boulangerite, tetrahedrite-tennantite, chalcostibite, zinkenite, famatinite); Fe-oxides: goethite and hematite.

These rocks were intruded by the Maronia pluton and the Ktismata microgranite porphyry, both of Oligocene age (Figure 2). The Maronia pluton consists mainly of shoshonitic monzogabbro and monzonite-quartz monzonite (hereafter, referred to as monzonite), as well as minor gabbroic bodies, and has a high-K calc-alkaline affinity and a subduction-related, sub-continental lithospheric mantle signature [30–32]. The pluton has a medium-grained, mainly equigranular texture and consists mainly of pyroxene, amphibole, biotite, plagioclase, K-feldspar and quartz, with accessory apatite, magnetite, titanite, ilmenite and zircon. Rb-Sr whole rock and biotite geochronology yielded ages from 29.8 ± 1.3 to 28.4 ± 0.9 Ma [31,33,34]. Fission-track studies of apatite from the pluton revealed an age

of 29.3 ± 2.0 Ma [35]. Uranium-Pb zircon dating of the pluton were interpreted as emplacement age between 29.76 ± 0.02 and 29.60 ± 0.02 Ma [32].

The Maronia pluton was intruded by the Ktismata microgranite, which is spatially and genetically related to the porphyry style Cu-Mo \pm Re \pm Au mineralization (Figure 2). The emplacement of the microgranite was structurally controlled by three sets of faults trending NE-SW, NW-SE, and WNW-ESE. Dips are mostly steep to vertical with a minor strike-slip component, and as a consequence the contacts between the two igneous intrusions are sharp and well-defined. According to Melfos et al. [11], the microgranite porphyry comprises phenocrysts of quartz, K-feldspar and plagioclase in a fine-grained matrix of quartz, plagioclase and K-feldspar. Argillic, sericitic, and propylitic alteration styles were initially recognized by Melfos et al. [11]. Magnetite, pyrite, chalcopyrite, and molybdenite are the main ore minerals. Molybdenite is enriched in Re, with concentrations reaching up to 2.88 wt. % Re [11,12]. Pyrrhotite and bismuthinite are minor minerals. Sphalerite, galena, cubanite, boulangerite, bournonite, tetrahedrite/tennantite, chalcostibite, zinkenite, and famatinite occur in the late high-sulfidation epithermal veins that crosscut the porphyry system [11].

Exploration drilling on the Maronia prospect conducted by the Hellenic Chemical Products and Fertilizers Co Ltd. in 1973 involved four drill holes comprising a total length of 550 m. Despite the encouraging Cu and Au grades, the project was terminated without any resource estimate or feasibility study, possibly because the Maronia prospect is located in an extensive archaeological site or because its immediate vicinity with the Aegean Sea. The cores do not exist anymore and only some reports describe the mineralogical and geochemical results of the drilling [11].

Surface samples contain as much as 5460 ppm Cu, 7600 ppm Mo, >1 ppm Re, 49 ppm Sb, 1.7 ppm Hg, 0.18 ppm Te, 0.9 ppm Ga, and 1 ppm Au [9,11]. Geochemical data from one drill core showed a 10 m intercept grading 2 wt. % Cu, 12 ppm Au, 17 ppm Ag, which was probably associated with the high-sulfidation epithermal overprint. This epithermal event was also characterized by the presence of famatinite, tennantite, and pyrophyllite [8,11]. Boiling was considered as the main mechanism of the ore mineral precipitation occurring at temperatures between 280 and 460 °C, and pressures from 150 to 510 bar [11].

3. Sampling and Analytical Methods

Surface sampling, with particular focus on spatial relationships among the various types of hydrothermal alteration in different rock types, was carried out in the Maronia porphyry system. A set of 20 samples was collected, representing mainly the intensively altered rocks. Older surface samples from a previous study [11] were also considered for the mineralogical composition of the alterations.

Alteration minerals were identified using an optical microscope, X-ray diffraction (XRD) (PHILIPS, Almelo, The Netherlands) and a scanning electron microscope (SEM) (JEOL Ltd, Tokyo, Japan). Polished thin sections and epoxy mounts were prepared for detailed petrographic observations. Scanning electron microscope analyses of minerals were conducted at the Aristotle University of Thessaloniki using a JEOL JSM-840A equipped with an OXFORD INCA 300 energy-dispersive X-ray spectrometer (EDS) (Oxford Instruments Ltd., Abingdon, UK) operating at 20 kV accelerating voltage and 0.4 mA probe current in the back-scattering electron (BSE) mode. The following standards were used: SiK α , AlK α and KK α , sanidine; CaK α , MgK α diopside; FeK α , hematite; MnK α , tephroite; TiK α , rutile; NaK α , albite; FK α , fluorite; ClK α , sylvite.

4. Results

4.1. Structural Control on the Mineralization

There is a close relationship of the Maronia detachment fault with the porphyry style mineralization. The approximately E-W striking fault that shallowly dips to the south (Figure 3a) marks the southernmost boundary of the extensive detachment fault system. The fault active from 42 to 12 Ma exhumed the Biala Reka-Kechros high-grade metamorphic core complex in the north [32,36]

(Figure 1). However, only upper crustal low-grade metamorphic rocks, which were described as part of the Circum Rhodope belt, were exhumed in the south [28]. Bonev et al. [29] suggested that the uppermost low-grade Mesozoic Circum Rhodope belt constitutes a part of the hanging wall of the Tertiary extensional detachment system, whereas the lower high-grade metamorphic basement forms the footwall.

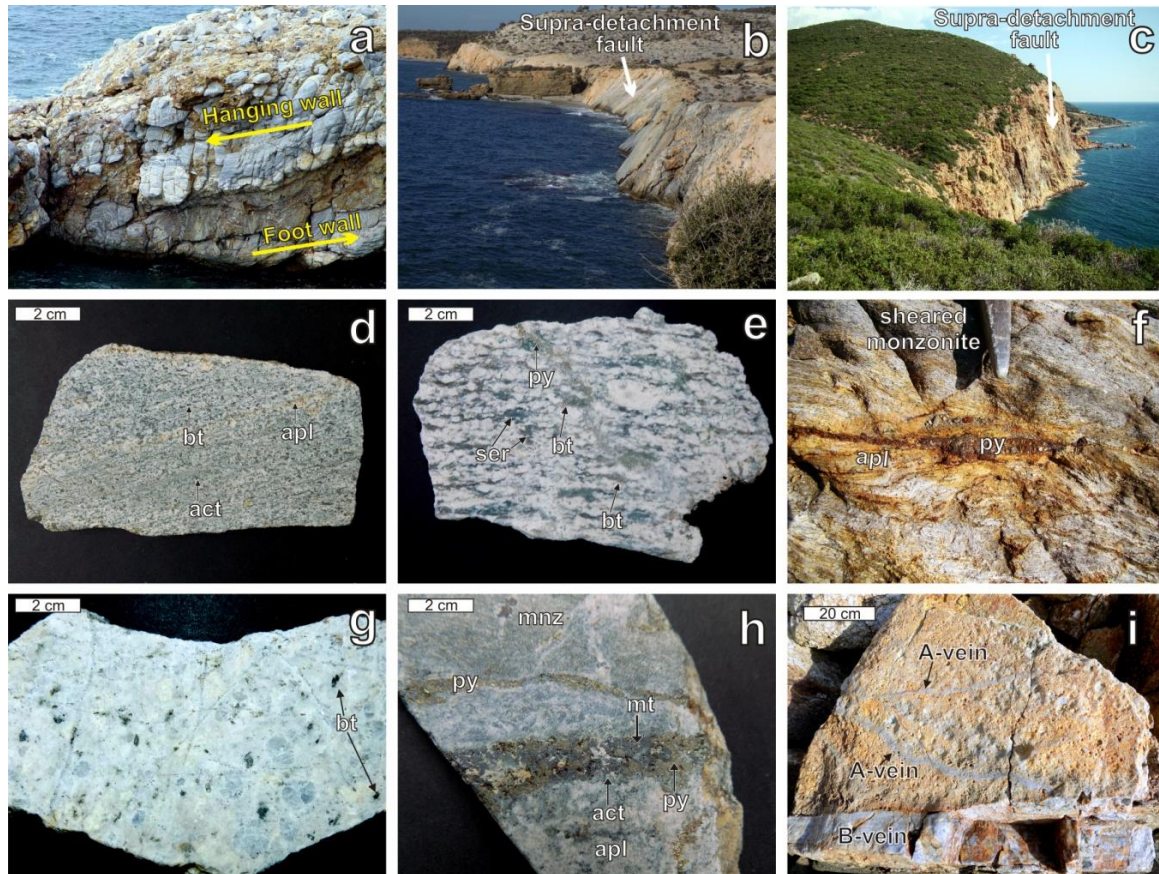


Figure 3. Photographs showing the structural control of the emplacement of the magmatic rocks, the potassic and sodic-calcic alterations with the associated mineralization and the various vein types. (a) The detachment fault is characterized by brecciation of the marble in the hanging wall and mylonitization of the calc-schist in the footwall (photographed towards SW); (b) High-angle supra-detachment normal fault in marble in the hanging wall of the detachment along the Aegean coast (photograph towards W); (c) High-angle supra-detachment normal fault along which the microgranite porphyry intruded (photographed towards E); (d) Sodic-calcic alteration consisting of hydrothermal actinolite (act) and biotite (bt) in highly strained and mylonitized monzonite, and an aplitic dike (apl) along the foliation; (e) Weak potassic alteration consisting of fine-grained hydrothermal biotite (bt) in highly strained microgranite porphyry, overprinted by strong sericitic alteration crosscut by a pyrite vein (py); (f) Mineralized aplitic dike (apl) that intruded mylonitized monzonite along the foliation; (g) Potassic alteration of the microgranite porphyry with secondary biotite (bt) at the south-eastern margin of the porphyry system; (h) M-type vein with hydrothermal magnetite (mt) and actinolite (act) associated with the sodic-calcic alteration in the sheared monzonite (mnz) and the aplitic dike (apl). Pyrite (py) (D-type vein) formed due to the re-opening of the vein during later sericitic alteration; (i) Barren A-type uninterrupted sinuous quartz veins associated with potassic alteration crosscut by a B-vein with pyrite-molybdenite mineralization in the microgranite porphyry.

Features that characterize the Maronia detachment include brecciation of the marble in the upper plate of the hanging wall, mylonitization of the calc-schist of the lower plate in the footwall (Figure 3a), and the listric and planar high-angle supra-detachment normal faults that affected metamorphic and

magmatic rocks along the Aegean coast (Figures 2 and 3b,c). These supra-detachment faults extend mainly SE–NW.

The Maronia microgranite porphyry was emplaced along the footwall of the detachment fault producing horizontal displacement along ductile to brittle shear zones. The most extended exposure of these shear zones occurs at the south-eastern margin of the porphyry system along the coast (Figure 2). In this site, monzonite and microgranite porphyry are highly strained and mylonitized with well-banded and linear textures (Figure 3d–f). Several aplitic dikes, from a few centimeters to more than 1 m thick, intrude the pluton and extend into the shear zone along ductile (Figure 3f) and brittle structures. These dikes are attributed to the intrusion of the microgranite porphyry along the foliation in the sheared monzonite. All these events demonstrate a syntectonic emplacement of the microgranite in the Maronia pluton. The aplitic-granitic dikes host miarolitic cavities with sulfides, suggesting volatile-rich residual melts exsolved from the granitic magma, which are probably related to the ore formation.

The following field and petrographic study are mainly based on new results but also considers previous research [11].

4.2. Potassic and Sodic-Calcic Hydrothermal Alteration

The hydrothermal alteration of the Maronia deposit is pervasive and consists of five main types in the microgranite and along the contacts with the monzonite. The alteration types include potassic, sodic-calcic, propylitic, sericitic, and argillic alteration, with local silicification (Figure 4). In this study, we focus on the potassic and sodic-calcic alteration.

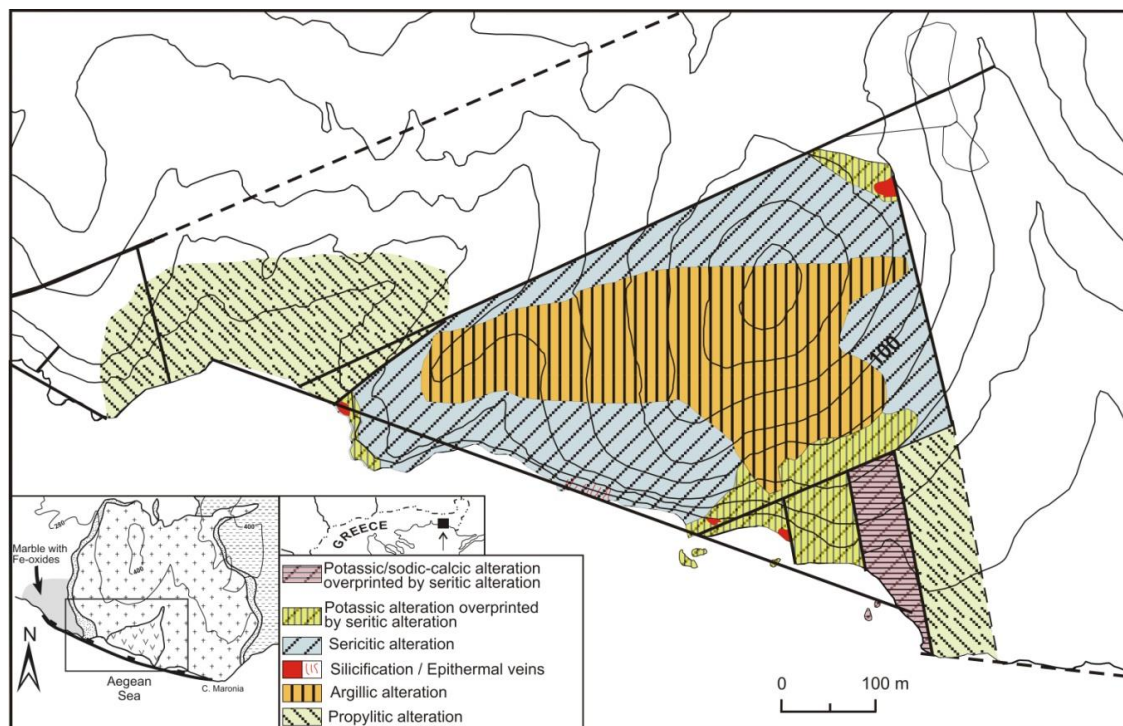


Figure 4. Distribution of the hydrothermal alteration zones at the Maronia porphyry system (modified after [11]).

Potassic alteration in most porphyry-style deposits has been coeval with sodic-calcic alteration (e.g., Yerrington porphyry Cu deposit, Nevada [37]; Ann-Mason porphyry Cu deposit, Nevada [38]; Vysoká–Zlatno Cu–Au skarn–porphyry deposit, Slovakia [39]), with fewer examples documenting their formation at different times (e.g., Gangdese porphyry copper belt, southern Tibet, China [40]). According to [9], many porphyry-style deposits in north-eastern Greece include varying proportions of

potassic, sodic and calcic alteration assemblages at the cores of the systems (e.g., Koryfes, Papadokoryfi, Pagoni Rachi, King Arthur, Myli).

At Maronia, mineral assemblages of these two alteration types do not demonstrate any clear temporal relationship, suggesting that they formed simultaneously. Weak potassic alteration is concentrated mainly in the northern, south-western, and south-eastern margins of the microgranite porphyry (Figures 3g and 4). However, a strong sodic-calcic alteration affected the monzonite and aplitic dikes along the south-eastern margin of the porphyry system (Figure 3f). At the south-eastern margin of the porphyry system, an apparent tectonic control on the potassic alteration occurs in the mylonitized microgranite porphyry and the sodic-calcic alteration in the mylonitized monzonite (Figure 3d–f). The potassic and sodic-calcic alteration assemblages in Maronia are superimposed by subsequent sericitic alteration (Figure 3e,g–i and Figure 4). The highest copper and molybdenum grades (up to 5460 ppm Cu and 7600 ppm Mo) are mainly associated with the zones of very dense quartz stockwork (e.g., silicification) in the potassic alteration.

4.3. Vein Types

New field observations revealed different types of veins associated with the alteration events in the Maronia deposit (Table 1). The mylonitized monzonite is crosscut by mineralized aplitic-granitic and microgranitic veins and dikes, varying in thickness from a few centimeters to 1 m, which host pyrite, chalcopyrite and pyrrhotite (Figure 3f). Additionally, a total of six early to late stage hydrothermal vein types were identified: M-, EB-, A-, B-, D- and epithermal-type veins, using the vein terminology proposed by [1]. Apart from the EB-veins, all the other veins do not exhibit alteration halos.

Table 1. Characteristics of veins in the alteration zones at Maronia. act: actinolite; ap: apatite; bt: biotite; cal: calcite; cpy: chalcopyrite; ep: epidote; ga: galena; Kfs: K-feldspar; mol: molybdenite; mt: magnetite; pl: sodic plagioclase; po: pyrrhotite; py: pyrite; pyr: pyrophyllite; qz: quartz; rt: rutile; ser: sericitic; sph: sphalerite; ss: Cu-Pb-(Sb + As) sulfosalts (bournonite, boulangerite, tetrahedrite-tennantite, chalcostibite, zinkenite, famatinite); tit: titanite.

Associated Vein Types	Alteration Type	Host Rock	Texture	Vein Assemblage	Sulfide Assemblage
M-type	Sodic-calcic	Monzonite	<5 cm wide	act + pl+ mt + tit ± cal ± ep	py
EB-type	Potassic	Monzonite and microgranite porphyry	1–5 mm wide, uninterrupted sinuous veins	bt + mt	-
A-type	Potassic	Microgranite porphyry	1–3 cm wide, uninterrupted sinuous veins-stockworks	bt + Kfs + mt + qz + rt ± ap	cpy + po + py
B-type	Potassic	Microgranite porphyry	1–3 cm wide, continuous straight veins-stockworks	bt + Kfs + mt + qz	cpy + mol + py
D-type	Sericitic	Microgranite porphyry	<10 cm wide, continuous straight veins	qz + ser	py
Epithermal-type	Advanced argillic	Microgranite porphyry	1–5 cm wide, continuous straight veins	qz + pyr	py + sph + ga + ss

Up to 5 cm wide M-type veins crosscut the monzonite and the aplitic dikes along the shear zone. These veins contain various proportions of secondary actinolite, sodic plagioclase, magnetite, epidote-allanite, calcite and titanite (Figure 3h), and are spatially coincident with the sodic-calcic

alteration, with which they are likely genetically related. Pyrite rarely occurs in M-type veins, but is present in the subsequent sericitic alteration overprint.

Early biotite (EB) veinlets (1–5 mm wide) consist of fine-grained biotite and magnetite (Figure 5a–c) and are spatially related to potassically altered microgranite porphyry (Figure 5b). A-type uninterrupted sinuous veins and B-type veins (1–3 cm wide) consist of granular quartz and occur in both the deformed and the undeformed parts of the potassically altered microgranite porphyry (Figure 3i). These veins are mostly barren but in places they contain sulfide mineralization consisting of pyrite + magnetite + chalcopyrite + pyrrhotite in the A-type veins, and pyrite + chalcopyrite + molybdenite in the B-type veins (Figure 3i).

A- and B-type quartz veins are crosscut by later D-veins, up to 10 cm wide (Figure 3h), which contain pyrite ± quartz typical of the sericite alteration at Maronia. Late epithermal-type quartz and pyrophyllite veins (1–5 cm wide) with variable concentration of sulfides (pyrite, sphalerite, galena) and Cu-Pb-(Sb + As) sulfosalts (boulangerite, famatinite, chalcostibite, Pb-tennantite, tetrahedrite, bournonite, zinkenite) occur on the southern and the south-eastern margins of the microgranite porphyry. They are related to the latest epithermal overprint [11,41] (Figures 2 and 4).

4.4. Mineral Composition and Chemistry of Potassic and Sodic-Calcic Alteration

Potassic alteration in the microgranite and the monzonite is characterized by secondary biotite + K-feldspar (orthoclase) + magnetite + rutile + quartz ± apatite. This alteration assemblage is the same in the two magmatic rocks, and only variations in the mineral proportions were observed, which are related to the alteration intensity. Sodic-calcic alteration in the monzonite is characterized by the assemblage of actinolite + sodic-calcic plagioclase (albite/oligoclase/andesine) + titanite + magnetite + chlorite + quartz ± calcite ± epidote-allanite.

Two types of biotite were analyzed: (1) primary magmatic biotite from the monzonite and (2) secondary biotite from the monzonite and the microgranite porphyry. Primary magmatic biotite forms platy crystals up to 3 mm in size in the monzonite matrix and is usually well preserved. However, in some places with sodic-calcic alteration, it was dissolved and newly alteration minerals in various amounts precipitated, mainly secondary chlorite, actinolite, and titanite (Figure 5a–c). Magmatic biotites plot in the phlogopite field of the Fe/(Fe + Mg) versus Al^{IV} diagram (Figure 6a). They are also characterized by a relatively high amount of TiO₂ (5.25 to 6.80 wt. %; 0.59 to 0.75 apfu) (Table 1, Figure 6b) and a negative correlation of Ti and Si (Figure 6c). Low Fe/(Fe + Mg) ratios (0.24–0.29) and variable chlorine concentrations (up to 0.34 wt. %) were observed. The MgO content varies between 15.49 and 17.25 wt. % and the Mg/(Mg + Fe) ratio from 0.71 to 0.76. Similar compositions of magmatic biotite in the monzonite at Maronia were reported by Papadopoulou [42]. For example, the TiO₂ content of biotite ranges from 4.37 to 6.49 wt. % and the Mg/(Mg + Fe) ratios from 0.55 to 0.76.

The most intense development of secondary biotite occurs at the eastern margin of the porphyry system along the sheared monzonite and microgranite porphyry. Macroscopically, the conversion of the greenish gray granular texture of the monzonite to a black biotite-rich mylonite (Figure 3d,f) is the most dramatic visual presentation of the hydrothermal biotite. It is distinguished from magmatic biotite by shreddy texture and fine-grained (typically <100 μm) anhedral morphology in the matrix where it occurs as disseminations, patches, small aggregate clusters or veinlets (EB-veins), up to 1 mm wide (Figure 5d–i). Hydrothermal biotite replaces primary magmatic pyroxene, biotite and hornblende in the monzonite (Figure 5d–f). It also forms veins and veinlets and fills interstices between phenocrysts in the microgranite (Figure 5g–i). Microscopically, hydrothermal biotite commonly co-exists with secondary magnetite, K-feldspar, rutile and quartz. Quartz and orthoclase rarely form alteration halos along the veinlets (Figure 5i).

The chemical composition of hydrothermal biotite is shown in Table 2 and Figures 6 and 7. In a plot of Fe/(Fe + Mg) versus Al^{IV}, the compositions of the biotite in the microgranite porphyry plot along the boundary between biotite and phlogopite fields (with Al^{IV} 1.54–2.10 apfu), whereas biotite in the monzonite partly overlaps the field of the magmatic biotite (Figure 6a). However, hydrothermal

biotite can be discriminated from the magmatic biotite by its lower Al^{IV} content (Figure 6a). The TiO₂ content is lower than that in the magmatic biotite, and similar to the biotite from the microgranite porphyry and monzonite. In both rock types, the hydrothermal biotite contains between 2.64 and 4.66 wt. % TiO₂, corresponding to 0.30–0.52 apfu Ti (Figure 6b,c).

Table 2. Representative microanalyses (wt. %) and calculated formulae of magmatic biotite from the monzonite (MA 8b) and hydrothermal biotite from microgranite porphyry (MA 11) and monzonite (MA 1, MA 8b) in Maronia. FeO*: total iron as FeO; bdl: below detection limit.

Biotite Type	Magmatic Biotite				Hydrothermal Biotite								
	Sample	MA 8b				MA 11				MR 1		MR 8b	
		8	9	14	15	1	10	15	22	3	5	1	10
SiO ₂	38.96	39.19	38.85	36.27	38.61	39.47	38.54	39.73	38.74	38.19	39.04	40.17	
TiO ₂	5.25	5.90	6.10	6.80	3.02	2.64	3.25	4.22	3.00	3.83	4.45	4.66	
Al ₂ O ₃	14.52	14.83	14.40	15.31	13.84	14.14	14.22	13.33	14.64	14.70	13.78	14.74	
Cr ₂ O ₃	0.44	0.86	0.04	0.04	bdl	0.16	0.24	bdl	0.24	0.35	1.07	0.37	
FeO*	9.69	9.82	10.68	11.47	16.62	14.43	13.72	12.22	9.99	11.74	10.60	8.88	
MnO	0.39	0.14	0.07	0.21	0.18	0.59	0.37	0.48	0.61	0.54	bdl	0.28	
MgO	17.25	16.85	16.84	15.49	14.03	15.32	14.22	15.60	18.22	16.45	17.31	17.53	
CaO	0.18	0.01	0.03	0.13	bdl	bdl	bdl	0.13	0.08	0.25	0.46	bdl	
Na ₂ O	0.39	0.32	0.06	0.37	0.43	0.23	0.02	bdl	0.26	0.20	0.36	0.20	
K ₂ O	9.47	8.73	9.47	9.01	9.58	9.56	10.06	9.52	9.09	9.76	9.30	9.29	
F	bdl	bdl	bdl	bdl	bdl	bdl	bdl	bdl	bdl	bdl	bdl	bdl	
Cl	0.01	bdl	0.05	0.23	0.11	0.02	0.10	0.30	bdl	0.19	0.09	bdl	
O = F, Cl	0.00	0.00	0.01	0.05	0.02	0.00	0.02	0.07	0.00	0.04	0.02	0.00	
Total _{initial}	96.55	96.65	96.59	95.33	96.42	96.56	94.74	95.53	94.87	96.20	96.46	96.12	
Fe ₂ O ₃ _{calc}	7.56	6.97	6.90	9.13	12.25	10.50	11.37	7.37	6.12	6.65	7.49	6.76	
FeO _{calc}	2.89	3.55	4.47	3.25	5.60	4.98	3.49	5.59	4.48	5.76	3.86	2.80	
H ₂ O _{calc}	2.39	2.31	2.16	2.20	3.01	3.07	3.02	2.71	2.91	2.67	2.49	2.64	
Total _{calc}	99.70	99.66	99.43	98.39	100.63	100.68	98.87	98.91	98.15	99.50	99.68	99.44	
Chemical formulae calculated on the basis of 22 (O, OH, Cl) anions													
Si	5.746	5.755	5.759	5.557	5.805	5.831	5.835	5.954	5.715	5.698	5.747	5.865	
Al ^{IV}	2.289	2.215	2.214	2.346	1.724	1.872	1.798	1.556	2.228	2.046	2.060	2.105	
Fe ³⁺	0.000	0.030	0.026	0.097	0.470	0.298	0.366	0.490	0.056	0.256	0.193	0.029	
Z	8.034	8.000	8.000	8.000	8.000	8.000	8.000	8.000	8.000	8.000	8.000	8.000	
Al ^{VI}	0.235	0.352	0.302	0.420	0.728	0.590	0.739	0.797	0.316	0.538	0.331	0.431	
Mg	3.713	3.657	3.717	3.638	3.192	3.357	3.281	3.640	3.962	3.692	3.672	3.791	
Fe ²⁺	0.839	0.770	1.067	1.048	1.384	1.168	1.293	0.829	0.743	0.873	0.707	0.743	
Fe ³⁺	0.356	0.406	0.231	0.324	0.235	0.317	0.078	0.213	0.432	0.337	0.405	0.312	
Ti	0.591	0.669	0.670	0.752	0.344	0.301	0.380	0.473	0.337	0.431	0.518	0.525	
Cr	0.052	0.100	0.004	0.005	0.000	0.019	0.029	0.000	0.000	0.041	0.124	0.043	
Mn	0.048	0.017	0.008	0.027	0.023	0.074	0.048	0.061	0.077	0.068	0.000	0.034	
Y	5.834	5.971	6.000	6.214	5.906	5.826	5.848	6.013	5.867	5.979	5.756	5.880	
K	1.831	1.680	1.778	1.663	1.758	1.805	1.887	1.693	1.762	1.813	1.826	1.755	
Na	0.111	0.090	0.016	0.110	0.125	0.066	0.005	0.000	0.073	0.059	0.102	0.055	
Ca	0.028	0.001	0.004	0.021	0.000	0.000	0.000	0.021	0.013	0.040	0.073	0.000	
X	1.970	1.772	1.799	1.793	1.883	1.871	1.893	1.714	1.848	1.912	2.002	1.811	
Cl	0.002	0.000	0.012	0.061	0.029	0.005	0.026	0.077	0.000	0.049	0.022	0.000	
OH	2.356	2.267	2.488	2.252	3.023	3.029	3.050	2.709	2.897	2.730	2.381	2.579	
O ²⁻	1.642	1.733	1.500	1.687	0.948	0.966	0.924	1.214	1.103	1.221	1.597	1.421	
Mg/(Mg + Fe _t)	0.76	0.75	0.74	0.71	0.60	0.65	0.65	0.70	0.76	0.72	0.74	0.78	
Fe _t /(Mg + Fe _t)	0.24	0.25	0.26	0.29	0.40	0.35	0.35	0.30	0.24	0.28	0.26	0.22	

calc: calculated; Fe_t: Fe total.

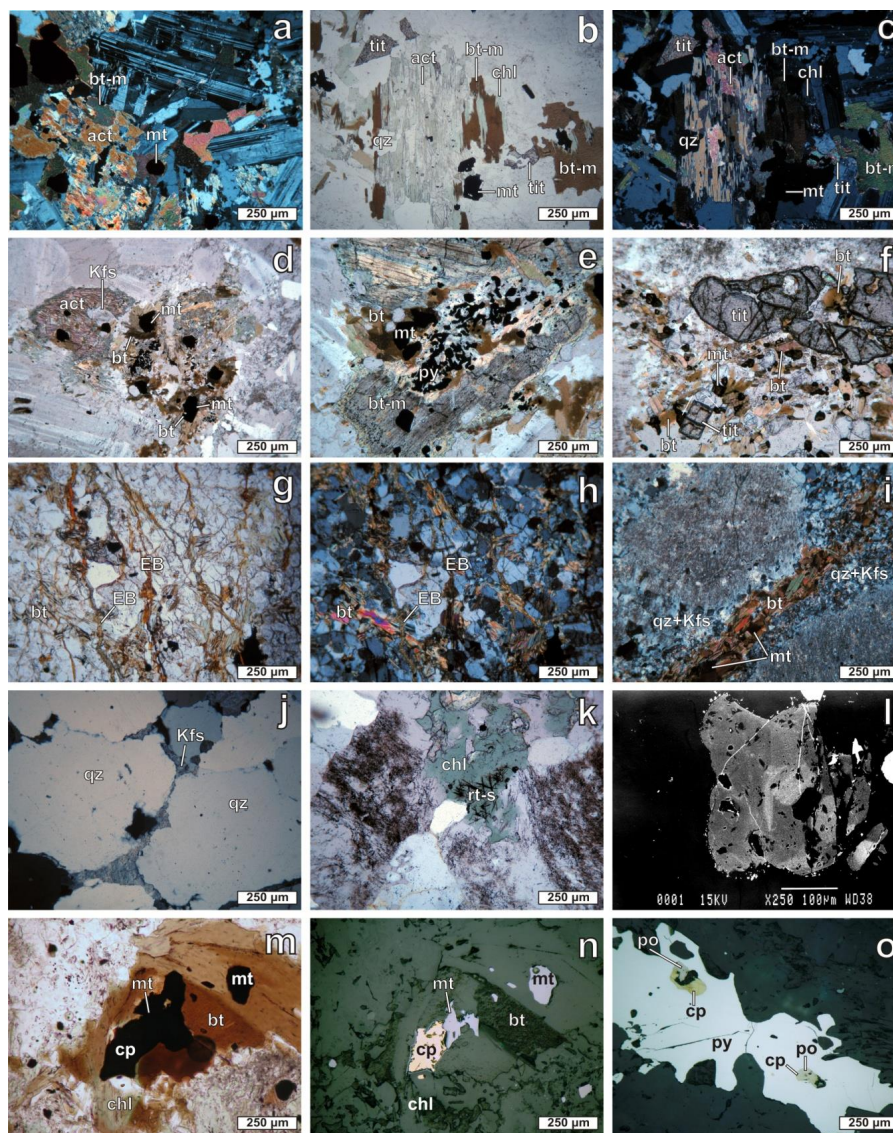


Figure 5. Photomicrographs of textures and minerals of the potassic and sodic-calcic alteration in the Maronia porphyry type mineralization. Plane polarized light: a, e, g, h, i, k, m; crossed-polarized light: b,c,d,f,j; plane reflected light images: n, o; SEM back-scattered image: l. (a) Magmatic biotite (bt-m) replaced by hydrothermal actinolite (act) and magnetite (mt) of the sodic-calcic alteration in the monzonite; (b,c) Magmatic biotite (bt-m) altered to hydrothermal actinolite (act), titanite (tit), chlorite (chl) and magnetite (mt) of the sodic-calcic alteration in the sheared monzonite; (d) Euhedral magmatic amphibole selectively altered to hydrothermal biotite (bt) and magnetite (mt). Primary K-feldspar (Kfs) is also present. Potassic alteration in the monzonite; (e) Magmatic biotite (bt-m) altered to hydrothermal biotite (bt), K-feldspar (Kfs), magnetite (mt) and pyrite (py) of the potassic alteration in the monzonite; (f) Hydrothermal titanite (tit), biotite (bt) and magnetite (mt) of the potassic alteration in the sheared monzonite; (g,h) EB-type veins (EB) and hydrothermal biotite (bt) of the potassic alteration in the microgranite porphyry; (i) Hydrothermal biotite (bt) and magnetite (mt) in EB-vein enveloped with a quartz-orthoclase (qz + Kfs) halo of the potassic alteration in the microgranite porphyry; (j) Hydrothermal orthoclase (Kfs) around granular quartz (qz) from the potassic alteration in microgranite porphyry; (k) Needle-like sagenitic rutile (rt-s) in chlorite (chl), which has totally replaced precursor magmatic biotite in potassic altered microgranite; (l) Rutile grain in potassic altered microgranite, showing sector zoning due to heterogeneous chemical composition. Brighter areas represent sectors with higher SrO contents (1.81–3.63 wt. %); (m,n) Chalcopyrite (cp) and magnetite (mt) associated with secondary biotite (bt) which is replaced by chlorite (chl), in potassic altered microgranite; (o) Chalcopyrite (cp) and pyrrhotite (po) inclusions in pyrite (py) as part of the potassic alteration mineral assemblage, in microgranite.

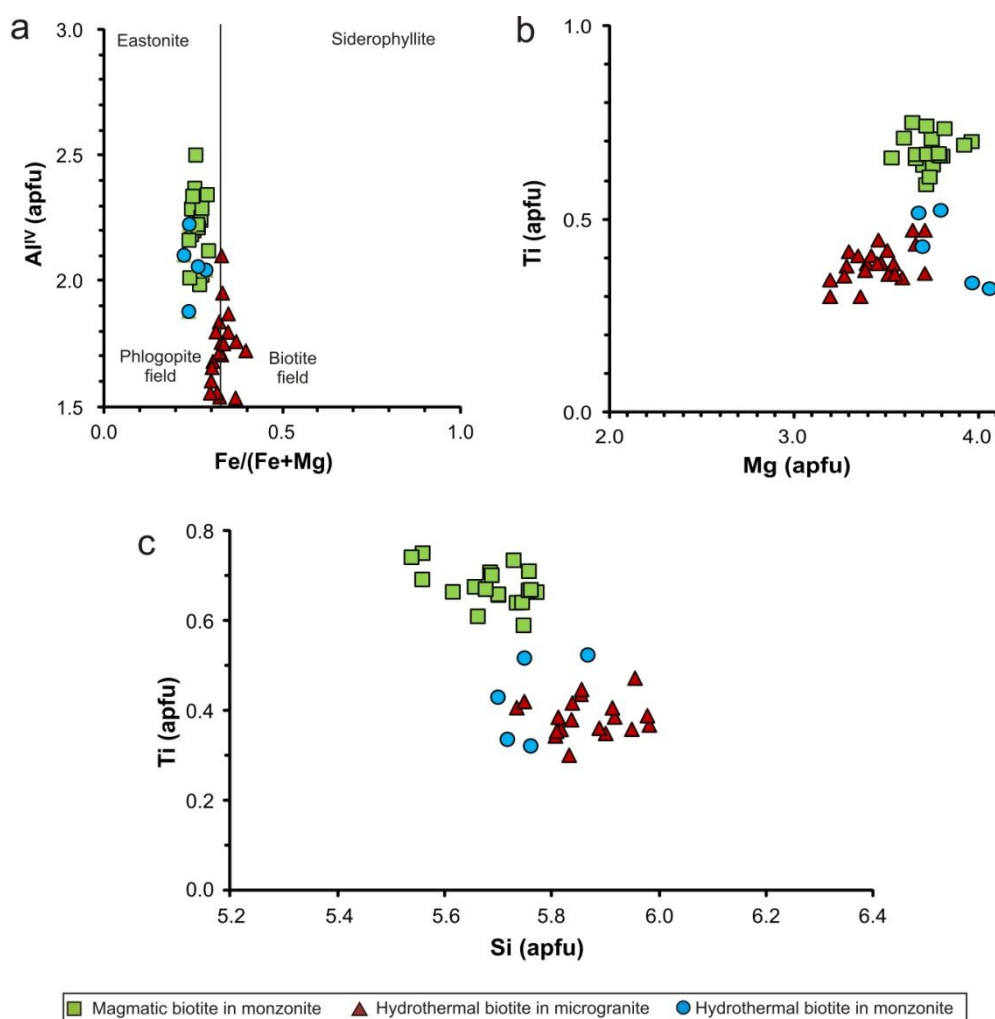


Figure 6. (a) Fe/(Fe + MgO) versus Al^{IV} diagram (after [43]), (b) Mg apfu versus Ti apfu diagram and (c) Si apfu versus Ti apfu diagram of the magmatic and hydrothermal biotite at the Maronia porphyry system. apfu, atoms per formula unit.

The MgO contents range from 14.03 to 16.22 wt. % (3.19–3.71 apfu Mg) in the hydrothermal biotite from microgranite porphyry and from 16.45 to 18.22 wt. % (3.69–3.96 apfu Mg) in the hydrothermal biotite in monzonite. Magnesium from hydrothermal biotite in microgranite porphyry and monzonite, plots in restricted compositional fields, and partly overlap that of magmatic biotite in monzonite (Figure 6b).

A negative correlation between Ti and Si occurs in hydrothermal biotite, but it is not as significant as in the magmatic biotite (Figure 6c). Similar negative correlations of magmatic and hydrothermal biotite were observed in porphyry deposits elsewhere (e.g., [44,45]). The higher SiO_2 content in the secondary biotite from the microgranite can be explained by the removal of Si from the quartz-rich host granitic rock. Up to 0.38 wt. % Cl contents in hydrothermal biotite overlap those of magmatic biotite (up to 0.34 wt. % Cl). The Fe/(Fe + Mg) ratio of the hydrothermal biotite in microgranite porphyry ranges from 0.30 to 0.40 and is relatively higher than that of the magmatic biotite (Figure 6a). However, the ratio in hydrothermal biotite from the monzonite ($Fe/(Fe + Mg) = 0.22$ – 0.28) overlaps with that in magmatic biotite.

The ternary diagram $10 \times TiO_2$ –(FeO + MnO)–MgO proposed by Nachit et al. [46], is used here as a quantitative geochemical tool for discriminating the primary magmatic biotites from those that are newly formed (neofomed) by the action of the hydrothermal fluids. Biotites from Maronia plot in the fields of magmatic and newly formed hydrothermal biotites, demonstrating their different origin

(Figure 7). However, the composition of hydrothermal biotite from the microgranite porphyry is indistinguishable from the hydrothermal biotite in the monzonite. Therefore, all the newly grown biotites in the potassic alteration stage probably formed in equilibrium with the hydrothermal fluids. Similar geochemical behavior has been observed in hydrothermal biotites from other porphyry deposits [47].

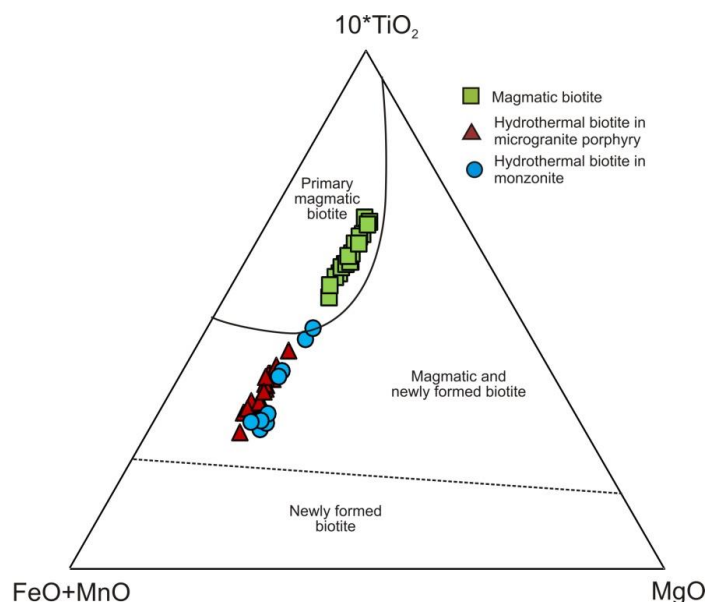


Figure 7. Ternary $10 \times \text{TiO}_2$ -(FeO + MnO)-MgO composition of magmatic biotites from the monzonite and secondary biotites from the potassic alteration of the monzonite and the microgranite porphyry in Maronia. The discrimination field boundaries are from Nachit et al. [46]. Total iron as FeO.

Subhedral to anhedral grains of K-feldspar in the potassic alteration of the Maronia porphyry system is mainly orthoclase, which is commonly intergrown with biotite, magnetite, quartz and pyrite. In EB-type veins, orthoclase-quartz assemblages may form alteration halos around biotite (Figure 5i). Orthoclase occurs interstitially around quartz grains in potassically altered microgranite porphyry (Figure 5j). Microanalyses show that the hydrothermal K-feldspar has a composition ranging from Or₈₁ to Or₉₇ (Table 3, Figure 8).

Rutile, which is associated with potassic alteration occurs as disseminated grains up to 0.5 mm in size or more rarely as tiny needle-like sagenite with chlorite in magmatic biotite precursor (Figure 5k,l). Rutile is mainly concentrated along the south-eastern margin of the porphyry system, in the monzonite and microgranite porphyry. It contains elevated concentrations of Sr (SrO up to 3.63 wt. %), W (WO₃ up to 2.33 wt. %) and Nb (Nb₂O₅ from 0.17 to 1.15 wt. %), and high Pb (Pb up to 0.16 wt. %), V (V₂O₅ up to 0.29 wt. %), Y (Y₂O₃ up to 0.12 wt. %) (Table 4). Rutile crystals generally exhibit well-developed zoning patterns with sectors of heterogeneous chemical composition related to the enrichment of several minor elements (Figure 5l). These elements were incorporated into the rutile lattice during crystal growth resulting in a sector-zoning pattern, which has previously been described by Rabbia et al. [48] and Rabbia and Hernandez [49] at porphyry-type deposits elsewhere. The light grey zones as revealed by SEM-back scattering images (BSE) are related to high Sr concentrations (SrO 1.81–3.63 wt. %).

Potassic alteration commonly contains magnetite and sulfides (pyrite, chalcopyrite, pyrrhotite) associated with secondary biotite (Figure 5m,n). Magnetite in the potassic alteration zone forms disseminated subhedral to anhedral grains (50–300 μm in size) that are mainly associated with biotite (Figure 5a–f,i,m–o). Magnetite is intergrown with pyrite, chalcopyrite and pyrrhotite (Figure 5m,n). Chalcopyrite is an abundant sulfide in potassically altered rocks and occurs mainly as disseminated anhedral grains (10–500 μm in size) within pyrite grains. It is intergrown with magnetite, pyrite, and pyrrhotite (Figure 5m–o).

Table 3. Representative microanalyses (wt. %) and calculated formulae of hydrothermal K-feldspar in potassic alteration zone in the Maronia deposit. FeO*: total iron as FeO; bdl: below detection limit.

Sample	MA 8b	MA 8b	MA 8b	MA 11	MA 11	MA 11
	1	2	3	1	2	3
SiO ₂	62.44	62.81	63.04	64.83	64.85	62.65
TiO ₂	bdl	bdl	bdl	bdl	bdl	bdl
Al ₂ O ₃	18.79	18.87	18.45	18.10	17.93	18.60
FeO*	0.23	0.24	0.55	0.21	0.42	0.36
MnO	bdl	bdl	bdl	bdl	bdl	bdl
MgO	bdl	bdl	bdl	bdl	bdl	bdl
CaO	0.26	bdl	bdl	0.05	bdl	0.21
Na ₂ O	1.11	2.10	0.90	0.65	1.02	0.23
K ₂ O	13.84	12.53	14.61	15.91	15.17	15.42
BaO	2.85	3.13	2.50	bdl	0.42	2.45
Total	99.52	99.68	100.05	99.75	99.81	99.92
Chemical formulae calculated on the basis of 8 O anions						
Si	2.944	2.947	2.957	3.002	3.003	2.950
Ti	0.000	0.000	0.000	0.000	0.000	0.000
Al	1.044	1.043	1.020	0.988	0.978	1.032
Fe ³⁺	0.009	0.009	0.022	0.008	0.016	0.014
Z	3.997	3.999	3.998	3.998	3.998	3.997
Mn	0.000	0.000	0.000	0.000	0.000	0.000
Mg	0.000	0.000	0.000	0.000	0.000	0.000
Ca	0.013	0.000	0.000	0.003	0.000	0.010
Na	0.101	0.191	0.082	0.058	0.092	0.021
K	0.832	0.750	0.874	0.940	0.896	0.926
Ba	0.053	0.058	0.046	0.000	0.008	0.045
X	0.999	0.998	1.002	1.001	0.996	1.002
Or (mol. %)	89	81	92	94	91	97
Ab (mol. %)	10	19	8	6	9	2
An (mol. %)	1	0	0	0	0	1

Disseminated euhedral to subhedral prismatic crystals of hydrothermal actinolite, up to 0.5 mm in length, are associated with the sodic-calcic alteration in the monzonite. Actinolite replaced magmatic biotite and pyroxene, and coexists with hydrothermal plagioclase, titanite, epidote-allanite, magnetite, calcite and chlorite (Figure 5a–c). It is the main mineral phase in actinolite + magnetite ± pyrite ± epidote-allanite ± titanite M-type veins (Figure 3h). Microanalyses show a typical actinolite composition (Table 5), with CaO ranging from 12.41 to 13.80 wt. % and MgO from 19.68 to 19.82 wt. %. Ferric iron was estimated using the method of Schumacher [50]. All analyzed amphiboles belong to the calcic group with $(Ca + Na)_B \geq 1.00$ and $(Na + K)_A < 0.50$. Fe/(Fe + Mg) ratios are low and range from 0.16 to 0.17.

Table 5. Representative microanalyses (wt. %) and calculated formulae of hydrothermal actinolite in sodic-calcic alteration in the Maronia deposit. FeO*: total iron as FeO; bdl: below detection limit.

Samle	MA 8	MA 8	MA 11					
	1	2	1	2	3	4	5	6
SiO ₂	54.96	55.12	55.67	54.99	55.10	55.02	55.06	55.07
TiO ₂	0.11	0.70	0.23	0.56	0.17	0.54	0.41	0.22
Al ₂ O ₃	2.16	1.87	1.96	2.09	1.89	1.97	2.11	1.91
FeO*	6.65	6.84	6.98	6.84	6.89	7.23	6.78	7.45
MnO	0.49	0.17	0.31	0.23	0.29	0.17	0.39	0.24
MgO	19.68	19.82	19.77	19.70	19.78	19.80	19.69	19.82
CaO	12.41	13.80	12.89	13.23	13.76	12.55	12.69	13.45
Na ₂ O	0.48	0.19	0.31	0.42	0.28	0.25	0.22	0.35
K ₂ O	bdl	0.20	bdl	0.10	bdl	0.11	bdl	0.07
Cl	0.11	0.02	0.07	0.08	0.06	0.02	0.11	0.02
Total _{initial}	97.03	98.73	98.17	98.22	98.21	97.66	97.44	98.60
Final wt. % values								
MnO	0.49	0.17	0.31	0.23	0.29	0.17	0.39	0.24
FeO	5.12	6.84	5.38	6.24	6.89	6.07	5.67	5.62
Fe ₂ O ₃	1.70	0.00	1.78	0.67	0.00	1.29	1.24	2.04
H ₂ O ⁺	2.12	2.13	2.13	2.12	2.12	2.14	2.12	2.13
Total _{calc}	99.32	100.86	100.48	100.41	100.33	99.93	99.68	100.93
Chemical formulae calculated on the basis of 23 O anions								
Si	7.726	7.678	7.736	7.679	7.713	7.703	7.717	7.658
Al	0.274	0.307	0.264	0.321	0.287	0.297	0.283	0.313
Ti	0.000	0.015	0.000	0.000	0.000	0.000	0.000	0.023
Fe ³⁺	0.000	0.000	0.000	0.000	0.000	0.000	0.000	0.006
T	8.000	8.000	8.000	8.000	8.000	8.000	8.000	8.000
Ti	0.012	0.059	0.024	0.059	0.018	0.057	0.043	0.000
Al	0.083	0.000	0.057	0.023	0.025	0.028	0.066	0.000
Fe ³⁺	0.180	0.000	0.187	0.070	0.000	0.136	0.130	0.207
Fe ²⁺	0.601	0.797	0.625	0.729	0.807	0.647	0.646	0.653
Mn ²⁺	0.000	0.020	0.012	0.018	0.023	0.000	0.000	0.028
Mg	4.124	4.116	4.096	4.101	4.128	4.132	4.114	4.109
C	5.000	4.992	5.001	5.000	5.001	5.000	4.999	4.997
Mn ²⁺	0.058	0.000	0.025	0.009	0.011	0.020	0.046	0.000
Fe ²⁺	0.001	0.000	0.000	0.000	0.000	0.063	0.018	0.000
Ca	1.869	2.000	1.919	1.980	1.989	1.883	1.906	2.000
Na	0.072	0.000	0.056	0.011	0.000	0.034	0.030	0.000
B	2.000	2.000	2.000	2.000	2.000	2.000	2.000	2.000
Ca	0.000	0.060	0.000	0.000	0.075	0.000	0.000	0.004
Na	0.059	0.051	0.028	0.103	0.076	0.034	0.030	0.094
K	0.000	0.036	0.000	0.018	0.000	0.020	0.000	0.012
A	0.059	0.147	0.028	0.121	0.151	0.054	0.030	0.110
OH	1.974	1.995	1.984	1.981	1.986	1.995	1.974	1.995
Cl	0.026	0.005	0.016	0.019	0.014	0.005	0.026	0.005
W	2.000	2.000	2.000	2.000	2.000	2.000	2.000	2.000
Sum T, C, B, A	15.059	15.139	15.029	15.121	15.152	15.054	15.029	15.107
(Ca + Na) _B	1.99	2.06	2.00	2.00	2.06	1.94	1.96	2.00
(Na + K) _A	0.00	0.09	0.00	0.11	0.08	0.02	0.00	0.11
Fe/(Fe + Mg)	0.16	0.16	0.17	0.16	0.16	0.17	0.16	0.17
Mg/(Mg + Fe ²⁺)	0.91	0.84	0.88	0.86	0.84	0.91	0.90	0.86

Secondary plagioclase replaced magmatic plagioclase and potassium feldspar and is associated with hydrothermal actinolite, titanite, apatite, chlorite, and epidote-allanite in the sodic-calcic alteration. It forms unzoned euhedral to subhedral crystals up to 0.1 mm in length. Locally, it appears with chessboard-like twinning, which is common in sodic-calcic alteration of the porphyry systems, demonstrating that K-feldspar was replaced by sodic plagioclase [37]. Microanalyses showed an enrichment in Na (7.14 to 10.67 wt. % Na₂O) with a composition of plagioclase ranging between Ab₆₂ and Ab₉₁ (Table 6, Figure 8). This composition is very similar with the composition Ab₇₂ of oligoclase that was reported by Carten [37] in the sodic-calcic metasomatic zone in the Yerington porphyry Cu

deposit in Nevada (USA). Replacement of Ca by Na in plagioclase of the Maronia porphyry deposit is shown by the negative correlation of these two elements, which is similar to that reported by Carten [37] for secondary plagioclase in the Yerington deposit.

Table 6. Representative microanalyses (wt. %) and calculated formulae of hydrothermal plagioclase in sodic-calcic alteration at Maronia. FeO*: total iron as FeO; bdl: below detection limit.

Sample	MA 8	MA 11							
	43	1	2	3	4	13	14	15	16
SiO ₂	62.01	59.20	59.48	58.63	59.10	59.78	63.84	66.78	63.15
TiO ₂	bdl								
Al ₂ O ₃	23.60	25.08	25.14	26.04	24.84	24.79	22.43	20.61	23.18
FeO*	bdl	0.41	0.28	bdl	0.87	0.22	0.16	bdl	0.08
MnO	bdl								
MgO	bdl								
CaO	5.22	7.23	7.22	7.48	6.94	6.66	3.74	1.61	4.36
Na ₂ O	8.37	7.14	7.40	7.23	7.49	7.43	9.25	10.67	9.03
K ₂ O	0.39	0.38	0.12	0.20	0.06	0.43	0.45	0.24	0.34
BaO	0.23	0.34	0.02	0.11	0.51	0.39	0.11	bdl	bdl
Total	99.82	99.78	99.66	99.69	99.81	99.70	99.98	99.91	100.14
Chemical formulae calculated on the basis of 8 O anions									
Si	2.759	2.729	2.662	2.628	2.654	2.680	2.824	2.932	2.791
Al	1.237	1.254	1.326	1.376	1.315	1.310	1.169	1.067	1.207
Fe ³⁺	0.000	0.017	0.011	0.000	0.033	0.008	0.006	0.000	0.003
Ti	0.000	0.000	0.000	0.000	0.000	0.000	0.000	0.000	0.000
Z	3.997	4.001	3.999	4.004	4.002	3.998	4.000	3.998	4.001
Mn	0.000	0.000	0.000	0.000	0.000	0.000	0.000	0.000	0.000
Mg	0.000	0.000	0.000	0.000	0.000	0.000	0.000	0.000	0.000
Ca	0.249	0.267	0.346	0.359	0.334	0.320	0.177	0.076	0.207
Na	0.722	0.708	0.642	0.628	0.652	0.646	0.793	0.909	0.774
K	0.022	0.028	0.007	0.012	0.004	0.025	0.026	0.013	0.019
Ba	0.004	0.000	0.000	0.002	0.009	0.007	0.002	0.000	0.000
Or (mol. %)	3	3	1	1	1	3	3	1	2
Ab (mol. %)	72	62	64	63	65	65	79	91	77
An (mol. %)	25	35	35	36	34	32	18	8	21

Titanite is the dominant Ti-bearing phase in the Na-Ca-alteration assemblage at Maronia. It replaced magmatic minerals including magnetite, ilmenite, biotite and actinolite (Figure 5b,c). These minerals have already been reported from the monzonite [28]. Titanite forms distinctive elongated wedge-shaped crystals up to 1 mm in length (Figure 5d) and is associated with actinolite, magnetite, plagioclase and chlorite, and more rarely with epidote-allanite and calcite in the sodic-calcic alteration. Titanite contains 35.54 to 38.18 wt. % TiO₂ and 26.70 to 28.09 wt. % CaO (Table 7). The Al/Fe ratio varies from 1.8 to 3.8.

5. Discussion

5.1. Structural Control of Permeability and Fluid Flow

The Maronia porphyry system shares features in terms of age, geological and structural setting, hydrothermal alteration distribution, and alteration and ore mineralogy, to many Oligocene porphyry type deposits of the Biala Reka-Kechros metamorphic core complex in Greece (e.g., Pagoni Rachi, Konos Hill, Koryfes, Myli, Aisymi, King Arthur, St. Philippos and Papadokoryfi; [9,17]) (Figure 1). These deposits are related to magmas that were produced in a subduction-related magmatic arc. The magmas were transported to shallow depths through large detachment displacements at an extensional geotectonic regime that affected the Rhodope massif from the Eocene to Oligocene [8,9,20,27,32].

Two large magmatic intrusions occur in the Maronia area. Monzonite with a shoshonitic affinity of Oligocene age (28–30 Ma) was intruded by the younger microgranite [31,33]. The Cu-Mo ± Re

± Au mineralization is genetically related to the microgranite porphyry rather than the monzonite. The ascent of the magma to shallow levels was promoted by the low angle detachment fault in the Maronia area, which also acted as a conduit for the magmatic metalliferous fluids and volatiles.

Table 7. Representative microanalyses (wt. %) and calculated formulae of hydrothermal titanite in the sodic-calcic alteration at Maronia. FeO*: total iron as FeO; bdl: below detection limit.

Sample	MA 3a						
	2	3	4	5	6	7	8
SiO ₂	30.47	30.41	30.71	30.91	30.65	30.41	30.81
TiO ₂	37.39	37.47	35.54	36.76	38.18	37.27	35.96
Al ₂ O ₃	1.83	1.87	3.25	2.72	1.45	1.97	3.14
FeO*	0.89	0.94	1.23	1.02	1.13	1.39	1.89
MnO	bdl	0.18	0.31	bdl	0.20	0.10	0.04
MgO	0.19	bdl	bdl	bdl	0.11	0.21	0.06
CaO	27.88	27.04	27.20	28.09	27.86	26.70	27.32
Na ₂ O	bdl						
K ₂ O	bdl						
V ₂ O ₅	bdl	1.21	0.82	bdl	bdl	0.94	bdl
Total	98.65	99.12	99.06	99.50	99.58	98.99	99.22
Chemical formulae calculated on the basis of 5 O anions							
Si	1.007	0.995	1.006	1.011	1.005	0.998	1.012
Ti	0.929	0.922	0.875	0.904	0.942	0.919	0.888
Al	0.071	0.072	0.125	0.105	0.056	0.076	0.122
Y	1.000	0.994	1.001	1.009	0.998	0.996	1.010
Fe	0.025	0.026	0.034	0.028	0.031	0.038	0.052
Mn	0.000	0.005	0.009	0.000	0.006	0.003	0.001
Mg	0.009	0.000	0.000	0.000	0.005	0.010	0.003
Ca	0.987	0.948	0.954	0.984	0.979	0.938	0.961
Na	0.000	0.000	0.000	0.000	0.000	0.000	0.000
K	0.000	0.000	0.000	0.000	0.000	0.000	0.000
V	0.000	0.032	0.022	0.000	0.000	0.025	0.000
X	1.021	1.010	1.018	1.012	1.021	1.014	1.017
Fe/Al	0.35	0.36	0.27	0.26	0.55	0.50	0.43

The presence of plastic and cataclastic deformation features at the southeast margin of Maronia microgranite porphyry implies emplacement at the ductile-brittle transition, adjacent to the footwall of the Maronia detachment fault. This detachment produced ductile to brittle shear zones during emplacement of the granitic magma. Ductile deformation is expressed by the highly strained and mylonitized zones and the brittle deformation by the intense random veining of the system.

Fluids are transported through major conduits such as fractures in brittle crust [51–53], but they can also migrate through other high permeability conduits such as shear zones [54]. Cataclastic deformation increases significantly the permeability of the host rocks and thus promotes the fluid flow and evolution of the fluid-wallrock interaction. In contrast, the rocks have a low permeability in ductile conditions [53]. However according to Reynolds and Lister [55] and Weis [53], in the ductile regime, the temporally overpressured fluids result in an increase in the permeability of the rocks. In the case of Maronia, hot fluids migrated through the major shear zone, in a ductile-brittle transition regime and caused metasomatic reactions with the primary magmatic minerals of the host rocks that lead to potassic and sodic-calcic alteration. Similar conditions favored the formation of porphyry and epithermal deposits in the neighboring Biga peninsula of NW Turkey, which belong to the same geotectonic regime [27].

However, the change from ductile to brittle deformation was associated with a significant drop in fluid pressure, fracturation of the rock and permitted the escape of overpressured hydrothermal fluids and a rapid upward fluid flow. This process increases the volume of water, which interacts with the surrounding host rocks along the veins [55–57]. At Maronia, the high temperature M-, EB-, A- and

B-type veins and veinlets probably formed from an aqueous fluid phase, which percolated upward along the shear zone, shortly after magma was emplaced. This process has been previously described by Dilles [58] and Richards [56].

5.2. Hydrothermal Alteration

Hydrothermal alteration assemblages in the Maronia porphyry type deposit reflect fluid-rock interactions and multiple overlapping pulses of hydrothermal fluid flow through magmatic fluid discharge zones. The alteration zoning patterns that include potassic, sodic-calcic, propylitic, sericitic and argillic alterations correspond to the recently updated models proposed by Seedorff et al. [1] and Sillitoe [2]. According to these models, potassic alteration is the most promising ore indicator especially for Cu and Au. Sericite alteration overprints the previous potassic assemblages incorporating Mo and other metals, in addition to Cu and sometimes Au (e.g., Santa Rita in New Mexico [59]; Far Southeast in the Philippines [60]; El Teniente in Chile [61]). This is the reason why detailed mapping of the alteration zones at porphyry systems are in many cases a significant exploration tool, driven by the fact that large deposits are likely to be located at greater depths and costly deep exploration drilling is required.

Hydrothermal alteration in Maronia is genetically associated with the microgranite intrusion but it also extends into the adjacent monzonite. The deposit exhibits a nearly symmetrical pattern of alteration zoning. This symmetry is well expressed in the distribution of sericitic and argillic alterations (Figure 4) and is probably related to the relatively uniform texture of the microgranite and the lack of any significant tilting postdating the formation of the deposit. However, the distribution of the early potassic and sodic-calcic alterations is less symmetrical due to the apparent tectonic control (Figure 4). In addition, the intimate association of the early potassic with the sodic-calcic alteration, and the late sericitic alteration, indicates that the various alteration styles at Maronia developed as part of an evolving magmatic-hydrothermal system.

The sodic-calcic alteration typically postdates potassic alteration [2,19], but in Maronia, these two types of alterations are possibly contemporaneous, since there is not any clear evidence for the relative age from their distinctive mineral assemblages. Both alteration assemblages overprint each other, and secondary biotite, K-feldspar, magnetite and rutile of the potassic alteration coexist with hydrothermal actinolite, sodic-calcic plagioclase (albite/oligoclase/andesine) and titanite of the sodic-calcic alteration. This implies alkali exchange, with increase of Na, Ca and K and variable changes of Mg and Si as previously described by Seedorff et al. [1].

Potassic alteration formed in monzonite and microgranite, by addition of K, Fe and Mg, loss of Na and Ca and variable changes of Ti. These chemical modifications are reflected by the formation of hydrothermal biotite, orthoclase, magnetite, rutile, quartz, and apatite. In the monzonite, this association principally resulted from the reaction of magmatic hornblende, biotite and pyroxene to secondary biotite and of plagioclase to orthoclase. In microgranite porphyry, the newly formed secondary biotite developed due to the circulation of the high-temperature hydrothermal fluids along the grain boundaries. The main sulfide assemblage at the potassic alteration in Maronia includes pyrite, chalcopyrite and pyrrhotite, which are associated with hydrothermal biotite and magnetite.

The most significant chemical factor that distinguishes the two different types of biotite in Maronia is the decrease of Ti and the increase of Si from magmatic to hydrothermal biotite, especially in the microgranite porphyry (Figures 6 and 7). This is consistent with the results from porphyry Cu deposits elsewhere (e.g., in Santa Rita [44]; in Christmas and Elly [62]; in Bingham [63]; in Yerington [58]; in Koryfes, Pagoni Rachi, and Papadokoryfi [64–66]).

Conversely, hydrothermal biotite in the potassic alteration of monzonite at Maronia has a similar MgO content than magmatic biotite, but is slightly lower in hydrothermal biotite from the microgranite (Figure 6b). This is in agreement with Hendry et al. [62] who stated that in some porphyry systems (e.g., Christmas and Bingham) primary and secondary biotites have similar concentrations of magnesium, although most studies conclude that secondary biotite contains more MgO compared to magmatic

biotite [45,67–69]. The differences in composition between biotite from the microgranite and the monzonite in Maronia are probably attributed to changes in fluid composition with the mineralogical and geochemical variations of the two host magmatic rocks.

In the potassic alteration, the Fe/(Fe + Mg) ratio of hydrothermal biotite is low, reflecting high fO_2 , above the nickel-nickel oxide (NNO) buffer of the early high-temperature aqueous hydrothermal fluids in Maronia, similar to other porphyry Cu deposits [56,58,64,67,70]. The high-oxidizing conditions of the early aqueous fluids are also supported by the presence of hydrothermal magnetite, which is ubiquitous in the potassic and the sodic-calcic alteration zones of the Maronia system, similarly to other porphyry systems in northeastern Greece (e.g., Pagoni Rachi [17]). At those highly oxidized conditions in the potassic alteration, coarse-grained rutile formed due to the breakdown of pre-existing Ti bearing minerals in the monzonite, implying restricted Ti mobility under sub-solidus conditions [48,71]. Titanium is often regarded as an immobile element, and in porphyry systems it can be incorporated in hydrothermal minerals at high temperatures. This indicates that its solubility increases in aqueous fluids in the form of chlorides, fluorides, hydroxides or other complexes, and thus increasing its mobility [48,72]. This increase of Ti solubility and its transportation by the hydrothermal fluids may explain the presence of rutile in the microgranite. Titanium in the microgranite possibly originated from the dissolution of preexisting magmatic biotite and magnetite. The diversity and rarity of trace elements in rutile is due to the broad range of the composition of the fluids and the precursor minerals involved in the formation of rutile [49,71,73]. Potassic alteration in Maronia is characterized by rutile with elevated concentrations of Sr, W and Nb, and irregular amounts of Pb, V and Y. In addition, titanite (with 35.54–38.18 wt. % Ti) from the sodic-calcic alteration of fine monzonite could also contribute Ti for the formation of rutile during potassic alteration. Primary biotite broke down under the high-temperature potassic alteration conditions, and resulted in the exsolution as needle-like sagenitic rutile in chlorite, a process which has been previously described by Czamanske et al. [71] and Rabbia and Hernández [49] in porphyry type deposits.

Sodic-calcic alteration type in the monzonite contains only minor pyrite. It is characterized by secondary actinolite, albite/oligoclase/andesine, titanite, magnetite, chlorite, quartz, calcite and epidote-allanite. This mineral association, apart from magnetite, is similar to the S-2 alteration assemblage identified by Carten [37] and Dilles and Einaudi [38] for sodic-calcic alteration at the Yerington and the Ann-Mason porphyry Cu deposits. Magnetite has been determined at sodic-calcic zones in other porphyry systems, in Panguna (Papua New Guinea) and in El Teniente (Chile) [74,75] as well in Pagoni Rachi (Greece) [13,17].

The major reaction during this early alteration stage involved the conversion of magmatic biotite or pyroxene to actinolite implying an input of Ca in the hydrothermal fluids. Regardless of whether it was derived from biotite or pyroxene, the composition of secondary actinolite does not vary considerably. Additionally, the high albite component of hydrothermal plagioclase can be attributed to the introduction of Na into the system and the development of albite/oligoclase/andesine at the expense of magmatic calcic plagioclase (anorthite) during sodic metasomatism.

Titanite is a common phase in the sodic-calcic alteration associated with the Maronia deposit, implying that Ti and possibly part, or the entire, of Ca were released from primary magmatic minerals. Calcium can also be added externally, by basinal brines or carbonate rocks, which are penetrated by the ascending fluids. The main precursor to titanite could be primary biotite (with 2.87–6.80 wt. % Ti), magnetite (with 0.20–3.10 wt. % Ti), ilmenite (with 46.67–51.42 wt. % Ti), orthopyroxene (with 0.08–0.43 wt. % Ti), clinopyroxene (with up to 0.88 wt. % Ti), and/or amphibole (with 0.09–1.30 wt. % Ti) from the Maronia monzonite. The low Fe/Al ratio (Fe/Al = 0.3–0.6) in the studied titanite is compatible with the Fe/Al ratio of titanite from sodic-calcic alteration in porphyry Cu-Au deposits in British Columbia and indicated high fO_2 conditions of the fluids [76].

5.3. Formation Conditions of Potassic and Potassic/Sodic-Calcic Alteration

Oxidized felsic magmas, comparable with the granitic magma of Maronia, can produce fluids rich in K-Na capable to cause potassic and sodic alteration [56,77]. Although in some studies [38,78] basinal brines or meteoric fluids may have been involved in the genesis of sodic-calcic alteration, a magmatic origin of the fluids for this alteration style is not excluded (e.g., Lightning Creek, Northwest Queensland, Australia [79]). However, sodic-calcic alteration of K-rich magmatic rocks is possible when CO₂ is enriched in the magmatic fluids [79]. Previous fluid inclusion study indicates that the volatile fluids were vapor dominated and coexisted with brines with salinities of 28 to 55 wt. % NaCl equiv. and did not contain any appreciable CO₂ [11]. Therefore, in the Maronia deposit, the fluids possibly were enriched in Ca from an external source, either a basinal brine from outside of the magmatic fluid discharge zone, or a carbonate unit.

The high-oxidation state of the hydrothermal fluids resulted in the enrichment of metals in the aqueous phase, a process which has been previously described by Richards [23] and Sillitoe [3]. Chelle-Michou et al. [80] showed that the high-oxidation state of porphyry systems is associated with the deep crustal magmatic processes that control the behavior of S and the chalcophile metals. This high-oxidation state together with a pressure decrease probably favors the escape of H₂ gas and the subsequent dissociation of H₂O along with an increase of *f*O₂ [58,69,81]. Another likely cause for the high-oxidation state is the separation of sulfur from the magma under subsolidus magmatic-hydrothermal conditions and its partitioning into the aqueous fluid phase, a process that results in sulfur reacting with metals in the fluid to form sulfides (pyrite, chalcopyrite, pyrrhotite) and to release O₂ gas. The O₂ released from this reaction causes oxidation and breakdown of the magmatic ferromagnesian silicates as described for the Yerington porphyry Cu deposit by Dilles [58] and for the Bajo de la Alumbrera porphyry Cu-Au deposit [81]. The absence of anhydrite in the potassic alteration zone at Maronia is possibly attributed to low contents of sulfate sulfur species in the fluids. According to [1], sulfates, such as anhydrite, precipitate from oxidized sulfur, rather than reduced sulfur, which forms sulfide minerals.

Copper in the potassic alteration partitions into brine rather than the vapor phase at early stages of hydrothermal systems [81–83]. The presence of brine in Maronia is apparent from the fluid inclusion assemblage [11], and played a significant role in the precipitation of the A-type pyrite-magnetite-chalcopyrite-pyrrhotite quartz veins at temperatures between 320 and 450 °C (with a distinct peak at 400 °C) under boiling conditions. According to [81,84–86] Cu sulfides precipitate in potassic alteration zones under oxidizing conditions from brines, together with Fe minerals (e.g., magnetite). Copper and iron strongly tend to complex with Cl and partition into brine. The common chalcopyrite daughter crystals in the high salinity aqueous fluid inclusions of the veins at the potassic alteration in Maronia support this assumption.

6. Conclusions

The Maronia porphyry Cu-Mo ± Re ± Au mineralization is hosted in microgranite porphyry, which intruded the Oligocene monzonite, at the footwall of a detachment fault. This fault formed as a result of the extensional geotectonic regime in the Rhodope massif, which produced magmas in a subduction-related magmatic arc. The detachment and associated supra-detachment faults also acted as conduits of hydrothermal fluids and volatiles along ductile to brittle zones, which is expressed by intense shear and veining of the host rocks. Hot fluids migrated through the ductile to brittle shear zone at the south-eastern margin of the system and caused metasomatic reactions with the primary minerals of the microgranite porphyry and the adjacent monzonite. These reactions lead to potassic and sodic-calcic alteration. Brittle deformation also promoted the rapid upward flow of fluid, which interacted with the surrounding host rocks, along high permeability conduits, to form high temperature M-, EB-, A- and B-type veins. Magma that formed the Maronia microgranite had oxidized felsic affinity and produced fluids enriched in Na, Ca and K that are necessary to form the potassic and sodic-calcic alteration. The high-oxidation state of the hydrothermal fluids and the decrease in pressure resulted in

the enrichment of metals and sulfur in the aqueous phase. This process caused precipitation of sulfides (pyrite, chalcopyrite, pyrrhotite), O₂-gas release, and breakdown of the magmatic silicates to form the potassic and sodic-calcic alteration assemblages.

Author Contributions: Conceptualization, V.M. and P.V.; Data curation, V.M., P.V., M.M. and M.G.S.; Investigation, V.M., P.V., M.M. and M.G.S.; Methodology, V.M., P.V., M.M., M.G.S. and L.P.; Software, V.M. and M.M.; Validation, A.F., P.G.S., A.S., R.K., K.M.H., A.T. and C.M.; Writing—original draft, V.M. and M.M.; Writing—review & editing, P.V., M.G.S., L.P., A.F., P.G.S., A.S., R.K., K.M.H., A.T. and C.M. All authors have read and agreed to the published version of the manuscript.

Funding: A.T. was funded by CNRS-INSU (program CESSUR).

Acknowledgments: Two anonymous reviewers are kindly thanked for providing comments that significantly improved the manuscript. Cyril Chelle-Michou is sincerely thanked for his review and his constructive and valuable comments on an earlier version of this manuscript.

Conflicts of Interest: The authors declare no conflict of interest.

References

1. Seedorff, E.; Dilles, J.H.; Proffett, J.M., Jr.; Einaudi, M.T.; Zurcher, L.; Stavast, W.J.A.; Johnson, D.A.; Barton, M.D. Porphyry deposits: Characteristics and origin of hypogene features. In *Economic Geology 100th Anniversary Volume*; Hedenquist, J.W., Thompson, J.F.H., Goldfarb, R.J., Richards, J.P., Eds.; Economic Geology Publishing Company: Littleton, CO, USA, 2005; pp. 251–298.
2. Seedorff, E.; Barton, M.D.; Stavast, W.J.; Maher, D.J. Root zones of porphyry systems: Extending the porphyry model to depth. *Econ. Geol.* **2008**, *103*, 939–956. [[CrossRef](#)]
3. Sillitoe, R.H. Porphyry copper systems. *Econ. Geol.* **2010**, *105*, 3–41. [[CrossRef](#)]
4. Lowell, J.D.; Guilbert, J.M. Lateral and vertical alteration-mineralization zoning in porphyry ore deposits. *Econ. Geol.* **1970**, *65*, 373–408. [[CrossRef](#)]
5. Beane, R.E.; Titley, S.R. Porphyry copper deposits. Part II. Hydrothermal alteration and mineralization. In *Economic Geology 75th Anniversary Volume (1905–1980)*; Skinner, B.J., Ed.; Economic Geology Publishing Company: Littleton, CO, USA, 1981; pp. 235–269.
6. Sinclair, W.D. Porphyry deposits. In *Mineral Deposits of Canada: A Synthesis of Major Deposit-Types, District Metallogeny, the Evolution of Geological Provinces, and Exploration Methods*; Goodfellow, W.D., Ed.; Special Publication: London, UK, 2007; pp. 223–243.
7. Kesler, S.E.; Chryssoulis, S.L.; Simon, G. Gold in porphyry copper deposits: Its abundance and fate. *Ore Geol. Rev.* **2002**, *21*, 103–124. [[CrossRef](#)]
8. Melfos, V.; Voudouris, P. Cenozoic metallogeny of Greece and potential for precious, critical and rare metals exploration. *Ore Geol. Rev.* **2017**, *89*, 1030–1057. [[CrossRef](#)]
9. Voudouris, P.; Mavrogonatos, C.; Spry, P.G.; Baker, T.; Melfos, V.; Klemm, R.; Haase, K.; Repstock, A.; Djiba, A.; Bismayer, U.; et al. Porphyry and epithermal deposits in Greece: An overview, new discoveries, and mineralogical constraints on their genesis. *Ore Geol. Rev.* **2019**, *107*, 654–691. [[CrossRef](#)]
10. Voudouris, P.; Mavrogonatos, C.; Melfos, V.; Spry, P.G.; Magganis, A.; Alfieris, D.; Soukis, K.; Tarantola, A.; Periferakis, A.; Kołodziejczyk, J.; et al. The geology and mineralogy of the Stypsi porphyry Cu-Mo-Au-Re prospect, Lesvos Island, Aegean Sea, Greece. *Ore Geol. Rev.* **2019**, *112*, 103023. [[CrossRef](#)]
11. Melfos, V.; Vavelidis, M.; Christofides, G.; Seidel, E. Origin and evolution of the Tertiary Maronia porphyry copper-molybdenum deposit, Thrace, Greece. *Miner. Depos.* **2002**, *37*, 648–668. [[CrossRef](#)]
12. Voudouris, P.; Melfos, V.; Spry, P.G.; Bindi, L.; Moritz, R.; Ortelli, M.; Kartal, T. Extremely Re-Rich molybdenite from porphyry Cu-Mo-Au prospects in northeastern Greece: Mode of occurrence, causes of enrichment, and implications for gold exploration. *Minerals* **2013**, *3*, 165–191. [[CrossRef](#)]
13. Voudouris, P.; Melfos, V.; Spry, P.G.; Kartal, T.; Schleicher, H.; Moritz, R.; Ortelli, M. The Pagoni Rachi/Kirki Cu-Mo-Re-Au-Ag-Te deposit, northern Greece: Mineralogical and fluid inclusion constraints on the evolution of a telescoped porphyry-epithermal system. *Can. Mineral.* **2013**, *51*, 411–442. [[CrossRef](#)]
14. Voudouris, P.; Siron, C.R.; Márton, I.; Melfos, V.; Baker, T.; Spry, P.G. Eocene to Miocene hydrothermal deposits of northern Greece and Bulgaria: Relationships between tectonic-magmatic activity, alteration, and gold mineralization—A preface. *Soc. Econ. Geol. Guide Ser.* **2016**, *54*, 1–15.

15. Voudouris, P.; Melfos, V.; Spry, P.G.; Baker, T. Cenozoic porphyry-epithermal and other intrusion-related deposits in northeastern Greece: Geological, mineralogical and geochemical constraints. *Soc. Econ. Geol. Guide Ser.* **2016**, *54*, 43–82.
16. Voudouris, P.C.; Melfos, V.; Baker, T.; Spry, P.G. Diverse styles of Oligocene-Miocene magmatic-hydrothermal deposits in northeastern Greece: Relationships between tectonic-, magmatic activity, alteration and Au-Ag mineralization. *Soc. Econ. Geol. Guide Ser.* **2016**, *54*, 83–112.
17. Mavrogonatos, C.; Voudouris, P.; Berndt, J.; Klemme, S.; Zaccarini, F.; Spry, P.G.; Melfos, V.; Tarantola, Á.; Keith, M.; Klemm, R.; et al. Trace elements in magnetite from the Pagoni Rachi Porphyry prospect, NE Greece: Implications for ore genesis and exploration. *Minerals* **2019**, *9*, 725. [[CrossRef](#)]
18. Moshefi, P.; Hosseinzadeh, M.R.; Moayyed, M.; Lentz, D.R. Comparative study of mineral chemistry of four biotite types as geochemical indicators of mineralized and barren intrusions in the Sungun Porphyry Cu-Mo deposit, northwestern Iran. *Ore Geol. Rev.* **2018**, *97*, 1–20. [[CrossRef](#)]
19. Runyon, S.E.; Nickerson, P.A.; Seedorff, E.; Barton, M.D.; Mazdab, F.K.; Lecumberri-Sánchez, P.; Steele-MacInnis, M. Sodic-calcic family of alteration in Porphyry systems of Arizona And Adjacent New Mexico. *Econ. Geol.* **2019**, *114*, 745–770. [[CrossRef](#)]
20. Menant, A.; Jolivet, L.; Tuduri, J.; Loiselet, C.; Bertrand, G.; Guillou-Frottier, L. 3D subduction dynamics: A first-order parameter of the transition from copper- to gold-rich deposits in the eastern Mediterranean region. *Ore Geol. Rev.* **2018**, *94*, 118–135. [[CrossRef](#)]
21. van Hinsbergen, D.J.J.; Hafkenscheid, E.; Spakman, W.; Meulenkamp, J.E.; Wortel, R. Nappe stacking resulting from subduction of oceanic and continental lithosphere below Greece. *Geology* **2005**, *33*, 325–328. [[CrossRef](#)]
22. Jolivet, L.; Faccenna, C.; Huet, B.; Labrousse, L.; Le Pourhiet, L.; Lacombe, O.; Lecomte, E.; Burov, E.; Denèle, Y.; Brun, J.-P.; et al. Aegean tectonics: Strain localization, slab tearing and trench retreat. *Tectonophysics* **2013**, *597*, 1–33. [[CrossRef](#)]
23. Richards, J.P. Tectonic, magmatic, and metallogenic evolution of the Tethyan orogen: From subduction to collision. *Ore Geol. Rev.* **2015**, *70*, 323–345. [[CrossRef](#)]
24. Menant, A.; Jolivet, L.; Vrielynck, B. Kinematic reconstructions and magmatic evolution illuminating crustal and mantle dynamics of the eastern Mediterranean region since the late Cretaceous. *Tectonophysics* **2016**, *675*, 103–140. [[CrossRef](#)]
25. Blundell, D.; Arndt, N.; Cobbold, P.R.; Heinrich, C. 9: Processes of tectonism, magmatism and mineralization: Lessons from Europe. *Ore Geol. Rev.* **2005**, *27*, 333–349. [[CrossRef](#)]
26. Kaiser-Rohrmeier, M.K.; Von Quadt, A.; Driesner, T.; Heinrich, C.A.; Handler, R.; Ovtcharova, M.; Ivanov, Z.; Petrov, P.; Sarov, S.; Peytcheva, I. Post-orogenic extension and hydrothermal ore formation: High-precision geochronology of the central rhodopian metamorphic core complex (Bulgaria-Greece). *Econ. Geol.* **2013**, *108*, 691–718. [[CrossRef](#)]
27. Sánchez, M.G.; McClay, K.R.; King, A.R.; Wijbrams, J.R. Cenozoic crustal extension and its relationship to porphyry Cu-Au-(Mo) and epithermal Au-(Ag) mineralization in the Biga peninsula, northwestern Turkey. In *Tectonics and Metallogeny of the Tethyan Orogenic Belt*; Richards, J.P., Ed.; Society of Economic Geologists Special Publication: Littleton, CO, USA, 2016; Volume 19, pp. 113–156.
28. Meinhold, G.; Kostopoulos, D.K. The circum-rhodope belt, northern Greece: Age, provenance, and tectonic setting. *Tectonophysics* **2013**, *595*, 55–68. [[CrossRef](#)]
29. Bonev, N.; Marchev, P.; Moritz, R.; Collings, D. Jurassic subduction zone tectonics of the Rhodope Massif in the Thrace region (NE Greece) as revealed by new U-Pb and ⁴⁰Ar/³⁹Ar geochronology of the Evros ophiolite and high-grade basement rocks. *Gondwana Res.* **2015**, *27*, 760–775. [[CrossRef](#)]
30. Papadopoulou, L.; Christofides, G.; Bröcker, M.; Koroneos, Á.; Soldatos, T.; Eleftheriadis, G. Petrology, geochemistry and isotopic characteristics of the shoshonitic plutonic rocks from Maronia area, west Thrace, Greece. *Bull. Geol. Soc. Greece* **2001**, *34*, 967–976. [[CrossRef](#)]
31. Papadopoulou, L.; Christofides, G.; Koroneos, Á.; Bröcker, M.; Soldatos, T.; Eleftheriadis, G. Evolution and origin of the Maronia pluton, Thrace, Greece. *Bull. Geol. Soc. Greece* **2004**, *36*, 568–577. [[CrossRef](#)]
32. Perkins, R.J.; Cooper, F.J.; Condon, D.J.; Tattitch, B.; Naden, J. Post-collisional Cenozoic extension in the northern Aegean: The high-K to shoshonitic intrusive rocks of the Maronia Magmatic Corridor, northeastern Greece. *Lithosphere* **2018**, *10*, 582–601. [[CrossRef](#)]

33. Kyriakopoulos, K. A Geochronological, Geochemical and Mineralogical Study of Some Tertiary Plutonic Rocks of the Rhodope Massif and Their Isotopic Characteristics. Ph.D. Thesis, University of Athens, Athens, Greece, 1987. (In Greek).
34. Del Moro, A.; Innocenti, F.; Kyriakopoulos, C.; Manetti, P.; Papadopoulos, P. Tertiary granitoids from Thrace (Northern Greece): Sr isotopic and petrochemical data. *Neues Jahrb. Mineral. Abh.* **1988**, *159*, 113–135.
35. Biggazzi, G.; Del Moro, A.; Innocenti, F.; Kyriakopoulos, K.; Manetti, P.; Papadopoulos, P.; Norelli, P.; Magganis, A. The magmatic intrusive complex of Petrotta, West Thrace: Age and geodynamic significance. *Geol. Rhodopica* **1989**, *1*, 290–297.
36. Mposkos, E.D.; Kostopoulos, D.K. Diamond, former coesite and supersilicic garnet in metasedimentary rocks from the Greek Rhodope: A new ultrahigh-pressure metamorphic province established. *Earth Planet. Sci. Lett.* **2001**, *192*, 497–506. [[CrossRef](#)]
37. Carten, R.B. Sodium-calcium metasomatism; chemical, temporal, and spatial relationships at the Yerington, Nevada, porphyry copper deposit. *Econ. Geol.* **1986**, *81*, 1495–1519. [[CrossRef](#)]
38. Dilles, J.H.; Einaudi, M.T. Wall-rock alteration and hydrothermal flow paths about the Ann-Mason porphyry copper deposit, Nevada; a 6-km vertical reconstruction. *Econ. Geol.* **1992**, *87*, 1963–2001. [[CrossRef](#)]
39. Koděra, P.; Lexa, J.; Fallick, A.E. Formation of the Vysoká-Zlatno Cu-Au skarn-porphyry deposit, Slovakia. *Miner. Depos.* **2010**, *45*, 817–843. [[CrossRef](#)]
40. Lang, X.; Tang, J.; Li, Z.; Huang, Y.; Ding, F.; Yang, H.; Xie, F.; Zhang, L.; Wang, Q.; Zhou, Y. U-Pb and Re-Os geochronological evidence for the Jurassic porphyry metallogenic event of the Xiongkun district in the Gangdese porphyry copper belt, southern Tibet, PRC. *J. Asian Earth Sci.* **2014**, *79*, 608–622. [[CrossRef](#)]
41. Melfos, V.; Vavelidis, M.; Christofides, G. Cu-Pb-(Sb + As) sulphosalts from the porphyry type Cu-Mo (\pm Au) mineralization in Maronia area, Thrace county, Greece. In *Terranes of Serbia: The Formation of the Geologic Framework of Serbia and the Adjacent Regions*; Knezevic, V., Krstic, B., Eds.; Univeristy of Belgrade: Belgrade, Serbia, 1996; pp. 305–310.
42. Papadopoulou, L. Mineral Phase Equilibria, Crystallization Conditions and Evolution of the Maronia Pluton, Thrace, Greece. Ph.D. Thesis, Aristotle University of Thessaloniki, Thessaloniki, Greece, 2003. (In Greek).
43. Deer, W.A.; Howie, R.A.; Zussman, J. *An Introduction to the Rock Forming Minerals*, 2nd ed.; Longman: London, UK, 1992; p. 696.
44. Jacobs, D.C.; Parry, W.T. Geochemistry of biotite in the Santa Rita porphyry copper deposit, New Mexico. *Econ. Geol.* **1979**, *74*, 860–887. [[CrossRef](#)]
45. Selby, D.; Nesbitt, B.E. Chemical composition of biotite from the Casino porphyry Cu-Au-Mo mineralization, Yukon, Canada: Evaluation of magmatic and hydrothermal fluid chemistry. *Chem. Geol.* **2000**, *171*, 77–93. [[CrossRef](#)]
46. Nachit, H.; Ibhi, A.; Abia, E.H.; Ohoud, M.B. Discrimination between primary magmatic biotites, reequilibrated biotites and neofomed biotites. *Comptes Rendus Geosci.* **2005**, *337*, 1415–1420. [[CrossRef](#)]
47. Boomeri, M.; Nakashima, K.; Lentz, D.R. The Miduk porphyry Cu deposit, Kerman, Iran: A geochemical analysis of the potassic zone including halogen element systematics related to Cu mineralization processes. *J. Geochem. Explor.* **2009**, *103*, 17–29. [[CrossRef](#)]
48. Rabbia, O.M.; Hernández, L.B.; French, D.H.; King, R.W.; Ayers, J.C. The El Teniente porphyry Cu-Mo deposit from a hydrothermal rutile perspective. *Miner. Depos.* **2009**, *44*, 849. [[CrossRef](#)]
49. Rabbia, O.M.; Hernández, L.B. Mineral chemistry and potential applications of natural-multi-doped hydrothermal rutile from porphyry copper deposits. In *Rutile: Properties, Synthesis and Application*; Low, I.-M., Ed.; Nova Science Publishers: New York, NY, USA, 2012; pp. 209–228.
50. Schumacher, J.C. The estimation of the proportion of ferric iron in the electron-microprobe analysis of amphiboles. *Can. Mineral.* **1997**, *35*, 238–246.
51. Weis, P.; Driesner, T. The interplay of non-static permeability and fluid flow as a possible pre-requisite for supercritical geothermal resources. *Energy Procedia* **2013**, *40*, 102–106. [[CrossRef](#)]
52. Weis, P.; Driesner, T.; Coumou, D.; Geiger, S. Hydrothermal, multiphase convection of H₂O-NaCl fluids from ambient to magmatic temperatures: A new numerical scheme and benchmarks for code comparison. *Geofluids* **2014**, *14*, 347–371. [[CrossRef](#)]
53. Weis, P. The dynamic interplay between saline fluid flow and rock permeability in magmatic-hydrothermal systems. *Geofluids* **2015**, *15*, 350–371. [[CrossRef](#)]
54. Fossen, H.; Cavalcante, G.C.G. Shear zones—A review. *Earth Sci. Rev.* **2017**, *171*, 434–455. [[CrossRef](#)]

55. Reynolds, S.J.; Lister, G.S. Structural aspects of fluid-rock interactions in detachment zones. *Geology* **1987**, *15*, 362–366. [[CrossRef](#)]
56. Richards, J.P. Magmatic to hydrothermal metal fluxes in convergent and collided margins. *Ore Geol. Rev.* **2011**, *40*, 1–26. [[CrossRef](#)]
57. Halley, S.; Dilles, J.H.; Tosdal, R.M. Footprints: Hydrothermal alteration and geochemical dispersion around porphyry copper deposits. *Soc. Econ. Geol. Newsl.* **2015**, *100*, 12–17.
58. Dilles, J.H. Petrology of the Yerington Batholith, Nevada: Evidence for evolution of porphyry copper ore fluids. *Econ. Geol.* **1987**, *82*, 1750–1789. [[CrossRef](#)]
59. Reynolds, T.J.; Beane, R.E. Evolution of hydrothermal fluid characteristics at the Santa Rita, New Mexico, porphyry copper deposit. *Econ. Geol.* **1985**, *80*, 1328–1347. [[CrossRef](#)]
60. Hedenquist, J.W.; Arribas, A.; Reynolds, T.J. Evolution of an intrusion-centered hydrothermal system: Far Southeast-Lepanto porphyry and epithermal Cu-Au deposits, Philippines. *Econ. Geol.* **1998**, *93*, 373–404. [[CrossRef](#)]
61. Klemm, L.M.; Pettke, T.; Heinrich, C.A.; Campos, E. Hydrothermal evolution of the El Teniente deposit, Chile: Porphyry Cu-Mo ore deposition from low-salinity magmatic fluids. *Econ. Geol.* **2007**, *102*, 1021–1045. [[CrossRef](#)]
62. Hendry, D.A.F.; Chivas, A.R.; Long, J.V.P.; Reed, S.J.B. Chemical differences between minerals from mineralizing and barren intrusions from some North American porphyry copper deposits. *Contrib. Mineral. Petrol.* **1985**, *89*, 317–329. [[CrossRef](#)]
63. Bowman, J.R.; Parry, W.T.; Kropp, W.P.; Kruer, S.A. Chemical and isotopic evolution of hydrothermal solutions at Bingham, Utah. *Econ. Geol.* **1987**, *82*, 395–428. [[CrossRef](#)]
64. Voudouris, P. Mineralogical, Geochemical and Fluid Inclusion Studies on Epithermal Vein Type Gold/Silver Mineralizations at Kassiteres/Sapes, (NE-Greece). Ph.D. Thesis, University of Hamburg, Hamburg, Germany, 1993.
65. Voudouris, P. Mineral composition of mafic minerals and ore deposition from the Kassiteres (Sappes) and Pagoni Rachi (Kirki) porphyry Cu-Mo prospects/W.Thrace. *Bull. Geol. Soc. Greece* **2001**, *34*, 1005–1013. (In Greek)
66. Mavrogonatos, C.; Voudouris, P.; Spry, P.; Melfos, V.; Klemme, S.; Berndt, J.; Periferakis, A. Biotite chemistry from porphyry-style mineralization in Western Thrace, Greece. In Proceedings of the 8th Geochemistry Symposium, Antalya, Turkey, 2–6 May 2018; p. 193.
67. Moore, W.J.; Czamanske, G.K. Compositions of biotites from unaltered and altered monzonitic rocks in the Bingham Mining District, Utah. *Econ. Geol.* **1973**, *68*, 269–274. [[CrossRef](#)]
68. Taylor, R.P. Comparison of biotite geochemistry of Bakircay, Turkey, and Los Pelambres, Chile, porphyry copper systems. *Inst. Min. Metall. Trans.* **1983**, *92*, B16–B22.
69. Brimhall, G.H.; Crecar, D.A. Ore fluids: Magmatic to supergene. In *Thermodynamic Modeling of Geologic Materials. Minerals, Fluids, and Melts*; Carmichael, I.S.E., Eugster, H., Eds.; Mineralogical Society of America: Chantilly, VA, USA, 1987; Volume 17, pp. 235–321.
70. Chivas, A.R. Geochemical evidence for magmatic fluids in porphyry copper mineralization. *Contrib. Mineral. Petrol.* **1982**, *78*, 389–403. [[CrossRef](#)]
71. Czamanske, G.K.; Force, E.R.; Moore, W.J. Some geologic and potential resource aspects of rutile in porphyry copper deposits. *Econ. Geol.* **1981**, *76*, 2240–2246. [[CrossRef](#)]
72. Li, J.L.; Gao, J.; Klemd, R.; John, T.; Su, W. Fluid-mediated metal transport in subduction zones and its link to arc-related giant ore deposits: Constraints from a sulfide-bearing HP vein in lawsonite eclogite (Tianshan, China). *Geochim. Cosmochim. Acta* **2013**, *120*, 326–362. [[CrossRef](#)]
73. Meinhold, G. Rutile and its applications in earth sciences. *Earth Sci. Rev.* **2010**, *102*, 1–28. [[CrossRef](#)]
74. Ford, J.H. A chemical study of alteration at the Panguna porphyry copper deposit, Bougainville, Papua New Guinea. *Econ. Geol.* **1978**, *73*, 703–720. [[CrossRef](#)]
75. Cannell, J.; Cooke, D.R.; Walshe, J.L.; Stein, H. Geology, mineralization, alteration, and structural evolution of the El Teniente porphyry Cu-Mo deposit. *Econ. Geol.* **2005**, *100*, 979–1003. [[CrossRef](#)]
76. Celis, A. Titanite as an Indicator Mineral for Alkalic Cu-Au Porphyry Deposits in South Central British Columbia. Master's Thesis, University of British Columbia, Vancouver, BC, Canada, 2015.

77. Arancibia, O.N.; Clark, A.H. Early magnetite-amphibole-plagioclase alteration-mineralization in the Island copper porphyry copper-gold-molybdenum deposit, British Columbia. *Econ. Geol.* **1996**, *91*, 402–438. [[CrossRef](#)]
78. Battles, D.A.; Barton, M.D. Arc-related sodic hydrothermal alteration in the western United State. *Geology* **1995**, *23*, 913–916. [[CrossRef](#)]
79. Perring, C.S.; Pollard, P.J.; Dong, G.; Nunn, A.J.; Blake, K.L. The lightning creek sill complex, Cloncurry district, northwest Queensland: A source of fluids for Fe oxide Cu-Au mineralization and sodic-calcic alteration. *Econ. Geol.* **2000**, *95*, 1067–1089. [[CrossRef](#)]
80. Chelle-Michou, C.; Chiaradia, M.; Ovtcharova, M.; Ulianov, A.; Wotzlaw, J.F. Zircon petrochronology reveals the temporal link between porphyry systems and the magmatic evolution of their hidden plutonic roots (the Eocene Corocochuayco deposit, Peru). *Lithos* **2014**, *198*, 129–140. [[CrossRef](#)]
81. Proffett, J.M. Geology of the Bajo de la Alumbrera porphyry copper-gold deposit, Argentina. *Econ. Geol.* **2003**, *98*, 1535–1574. [[CrossRef](#)]
82. Hendry, D.A.F.; Gunow, A.J.; Smith, R.P.; Reed, S.J.B.; Long, J.V.P. Chemical differences between minerals from mineralizing and barren intrusions associated with molybdenum mineralization at Climax, Colorado. *Mineral. Petrol.* **1988**, *39*, 251–263. [[CrossRef](#)]
83. Lerchbaumer, L.; Audétat, A. High Cu concentrations in vapor-type fluid inclusions: An artifact? *Geochim. Cosmochim. Acta* **2012**, *88*, 255–274. [[CrossRef](#)]
84. Whitney, J.A.; Hemley, J.J.; Simon, F.O. The concentration of iron in chloride solutions equilibrated with synthetic granitic compositions: The sulfur-free system. *Econ. Geol.* **1985**, *80*, 444–460. [[CrossRef](#)]
85. Burnham, C.W. Magmas and hydrothermal fluids. In *Geochemistry of Hydrothermal Ore Deposits*, 3rd ed.; Barnes, H.L., Ed.; John Wiley and Sons: New York, NY, USA, 1997; pp. 63–123.
86. Seo, J.H.; Guillong, M.; Heinrich, C.A. Separation of molybdenum and copper in porphyry deposits: The roles of sulfur, redox, and pH in ore mineral deposition at Bingham Canyon. *Econ. Geol.* **2012**, *107*, 333–356. [[CrossRef](#)]



© 2020 by the authors. Licensee MDPI, Basel, Switzerland. This article is an open access article distributed under the terms and conditions of the Creative Commons Attribution (CC BY) license (<http://creativecommons.org/licenses/by/4.0/>).